Characterizing the Chiral Index of a Single-Walled Carbon Nanotube

*Qiuchen Zhao and Jin Zhang**

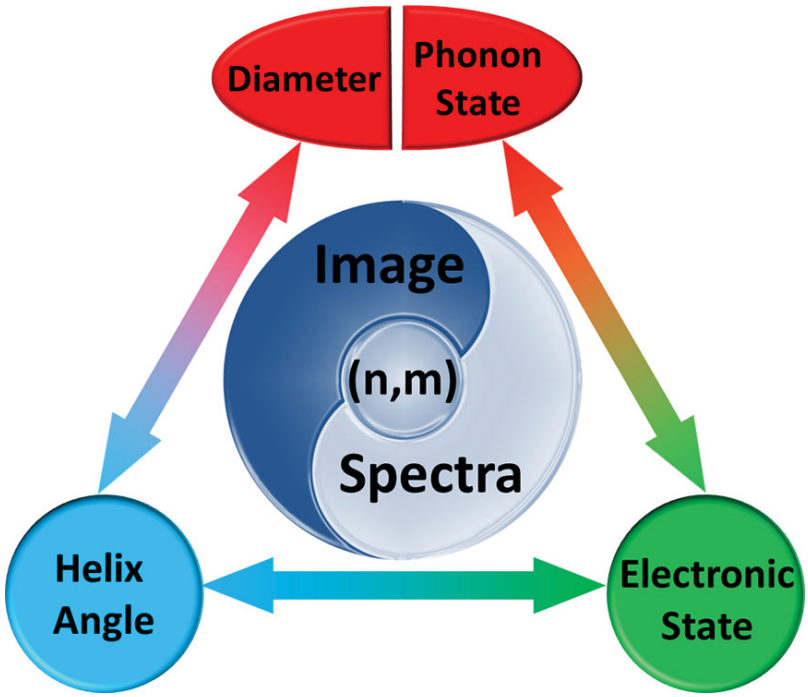

From the Contents

The properties of single-walled carbon nanotubes (SWCNTs) mainly depend on their geometry. However, there are still formidable difficulties to determine the chirality of SWCNTs accurately. In this review, some efficient methods to characterize the chiral indices of SWCNTs are illuminated. These methods are divided into imaging techniques and spectroscopy techniques. With these methods, diameter, helix angle, and energy states can be measured. Generally speaking, imaging techniques have a higher accuracy and universality, but are time-consuming with regard to the sample preparation and characterization. The spectroscopy techniques are very simple and fast in operation, but these techniques can be applied only to the particular structure of the sample. Here, the principles and operations of each method are introduced, and a comprehensive understanding of each technique, including their advantages and disadvantages, is given. Advanced applications of some methods are also discussed. The aim of this review is to help readers to choose methods with the appropriate accuracy and time complexity and, furthermore, to put forward an idea to find new methods for chirality characterization.

small NANO MICRO

1. Introduction

Single-walled carbon nanotubes (SWCNTs), a kind of one-dimensional carbon material with an elegant structure, have been well researched since their discovery in 1993.[1] According to theoretical calculations and experimental measurements, SWCNTs have fantastic properties for electrics, mechanics, thermotics, and optics.[2] Because of this, SWCNTs have multiple potential applications, including field-effect transistors (FETs),[3] logic circuits,[4] functional composites,[5] and sensors.[6] However, most of these properties depend on the special structure of the SWCNT, commonly defined as the chiral index (n, m). For example, when (n, m) mod 3 = 0, the SWCNT has metallic properties, or is semiconducting. The diversity of the SWCNT structure leads to major challenges for basic and applied research on SWCNTs. Many methods for SWCNT synthesis have been developed, such as arc discharge,[1,7] laser ablation,[8] and CVD processes,[9] but the obtained products are always a mixture of SWCNTs with different diameters and electronic properties, which limits their application.

Towards applications, to measure the precise structure of as-grown SWCNTs is meaningful. In order to characterize the overall morphology, one of the most convenient methods is scanning electron microscopy (SEM). Using SEM, we can observe the orientation and the position of SWCNTs,[10–12] the density of SWCNT horizontal arrays,[13–15] the alignment of SWCNTs in vertical arrays,[16–18] and the length of SWCNTs in ultra-long arrays.[19–21] It was also reported that using SEM can even differentiate metallic and semiconducting SWCNTs.[22] On the other hand, the length of a SWCNT can also be measured using optical methods with the help of TiO_2.[23] However, none of these methods can give us enough information about a specific single SWCNT.

Although a SWCNT could be very long, its diameter is usually in the range of 0.4 to 2 nm,[24] making it difficult to characterize. As properties of SWCNTs are determined by (n, m),[2] to characterize the chiral indices can give us much information on the structures and properties. Furthermore, a clear characterization of a SWCNT can help us understand the mechanism of SWCNT growth, for example, the chirality-dependent growth rate[25] and the formation of intramolecular junctions.[26,27]

Over the past 20 years, many techniques have been developed to characterize the chiral indices of SWCNTs, including imaging techniques and spectroscopy techniques. In the following parts, we will provide an overview of the main methods of characterizing the chiral indices of SWCNTs. In Section 2 we will discuss the definition of the (n, m) notation and the main idea for chiral index determination. The notation (n, m) is changed into measurable parameters, for example, diameter, helix angle, and electric state. In Sections 3 to 5, the practical measurements of the parameters which are mentioned in Section 2 are discussed. In Section 6, some chiral index determination examples are explained. A comparison and conclusion regarding the above-mentioned methods are then discussed in Section 7.

2. Theoretical Analysis for Chiral Index Determination

2.1. Structure of a Single-Walled Carbon Nanotube (SWCNT): (n, m) Notation

A SWCNT can be described as a single layer of graphene that is rolled up into a seamless one-atom-thick cylinder, usually with a small diameter along the circumference and a long length (micrometers to millimeters) along the cylinder axis.[28] Without regard to the length of the SWCNT along its cylinder axis, the structure of a SWCNT can be exclusively defined as a vector on the sheet of graphene, a so-called "chirality vector", $\mathbf{C}_h$:

$$C_h = na_1 + ma_2 \equiv (n, m) \quad (1)$$

where $\mathbf{a}_1$ and $\mathbf{a}_2$ are two unit vectors of the hexagonal honeycomb lattice. Both of the unit vectors are along the zigzag direction, and the two vectors have an included angle of 60°. $\mathbf{C}_h$ is usually perpendicular to the cylinder axis of the SWCNT. The angle between the chiral vector $\mathbf{C}_h$ and unit vector $\mathbf{a}_1$ is called the chiral angle, or helix angle, θ.[29] If $\theta = 0°$, the SWCNT is called a 'zigzag nanotube', and a SWCNT with $\theta = 30°$ is called an 'armchair nanotube'. SWCNTs with $0° < \theta < 30°$ are called chiral nanotubes. Furthermore, if n-m > 0, the nanotube is right-handed, and if n-m < 0, the nanotube is left-handed.[30]

2.2. The Main Ideas for (n, m) Determination

Current routes to characterize the chiral index of a SWCNT can be divided into two: imaging techniques and spectroscopy techniques. Imaging techniques, including atomic force microscopy (AFM), scanning tunneling microscopy (STM), transmission electronic microscopy (TEM), and electronic diffraction (ED), can directly give the diameter and the helix angle of a SWCNT. By these methods, we can usually get a clear image, and find the information by direct measurement. From spectroscopy techniques, including Raman spectroscopy, photoluminescence spectroscopy, and Rayleigh scattering microscopy, the phonon state and electronic state of a SWCNT can be obtained. We can get spectra at different wavelengths, and finally get the structures of SWCNTs with the help of theoretical calculations and fittings.

Q. Zhao, J. Zhang
Center for Nanochemistry
Beijing National Laboratory for Molecular Sciences
Key Laboratory for the Physics and
Chemistry of Nanodevices
State Key Laboratory for Structural
Chemistry of Unstable and Stable Species
College of Chemistry and Molecular Engineering
Peking University
Beijing 100871, P.R. China
E-mail: jinzhang@pku.edu.cn

DOI: 10.1002/smll.201401567

As mentioned in Section 2.1, n and m are two independent parameters, so, to determine the structure of a SWCNT, two independent parameters are necessary. We can get the diameter, phonon state, helix angle, and electronic state separately, and each two out of the three methods can determine the structure of a SWCNT. As phonon states and diameters are usually mutually dependent,[31] they are considered as one method in our discussion.

The diameter and the helix angle are geometrical properties of a SWCNT. With these two parameters, we can get an image of a SWCNT, so the characterization methods based on diameter (d) and helix angle (θ) measurements are called imaging techniques. Energy states, including electronic states and phonon states, however, are relatively abstract and usually require calculations before getting (n, m) notations. The information of these energy states is mainly given by spectroscopy methods, hence characterizations based on energy states are called spectroscopy techniques.

2.3. Imaging Techniques: (d,θ) Measurements

If the (n, m) notation can be regarded as a certain point in a two-dimensional cartesian coordinate system with an axis angle of 60°, we can make a polar coordinate transfer to use (L, θ) as the coordinate axis, as shown in **Figure 1**a. Then, we can use this expression of L and θ:

$$L = \sqrt{n^2 + nm + m^2} \tag{2}$$

$$\theta = arctan\left[\sqrt{3}m/(2n+m)\right] \tag{3}$$

where θ refers to the helix angle of a SWCNT. L has a linear relationship to the diameter:

$$d = \sqrt{3}a_{C-C} \times L/\pi \tag{4}$$

in which $a_{C\text{-}C}$ is the length of the C–C bonds (0.142 nm in graphite).[31] From Equations (2) to (4), we can see clearly that (d, θ) and (n, m) have a one-to-one correspondence. The detailed correspondence between (d, θ) and (n, m) is shown in Figure 1b.[32] In the (d, θ) plot, the horizontal axis is d while the vertical axis is θ. Points on the same curves in blue, purple, green, and black have the same value of m, n, (m+n), and (n-m). For example, the point in Figure 1b shows a (12, 7) tube, which is (1.30 nm, 21.4°) in (d, θ) notation.

2.4. Spectroscopy Techniques: $E_{eletronic}$ and E_{phonon} Measurements

2.4.1. Electronic Structure of a SWCNT

The electronic structure of a SWCNT is closely related to that of 2D graphene. The electronic energy surfaces of 2D graphene can be described by the nearest-neighbor tight binding (TB) model. The valence band and conduction band touch at two points of the hexagonal Brillouin zone, which are called the K points.[31] When rolling into a carbon nanotube, only certain quantized wave vectors are allowed due to quantum confinement:

$$k \cdot C_h = 2\pi q \tag{5}$$

Where k is the wave vector, and q is an integer. Because of this, the cutting lines of allowed wave vectors in the SWCNT reciprocal space can be represented in the 2D graphene sheet Brillouin zone, as shown in **Figure 2**c.[33] The solid curves show the cutting lines for the (4,2) nanotube. Figure 2d shows the electronic band structure of a SWCNT. We can classify SWCNTs into three parts, according to (m-n) MOD 3 = 0, 1, and 2. Since no allowed k vector crosses the K point, MOD 1 and MOD 2 SWCNTs are two types of semiconducting nanotubes, for they exhibit a chirality-dependent energy gap. In MOD 0 SWCNTs, a cutting line crosses the K point and thus these SWCNTs are classified as "metallic", for the density of states is continuous near the Fermi energy.

As C_h is related to the diameter, the energy function will also relate to the diameter, as shown in Equation (6). If we expand the function in Equation (6) in Taylor's series at 1/d = 0, we can get several expansion terms in Equations (7) and (8).

$$E = E(1/d) \tag{6}$$

$$= E(0) + E'(0)/d + E''(0)/d^2 + \ldots \tag{7}$$

$$= E_{graphene} + \alpha/d + \beta(\theta)/d^2 + \ldots \tag{8}$$

Qiuchen Zhao received his B.S. from Peking University in 2013. Since this, he has been a part of Prof. Jin Zhang's group working on a 5-year PhD program in College of Chemistry and Molecular Engineering, Peking University. His current research is focused on the structure-controlled synthesis of SWCNTs, especially on the mechanism of SWCNT growth, and kinetic models of the CVD process.

Jin Zhang received his PhD from Lanzhou University in 1997. After a postdoctoral fellowship at the University of Leeds, UK, he joined Peking University where he was appointed Associate Professor (2000), promoted to Full Professor in 2006, and then Cheung Kong Professor in 2013. His research focuses on the controlled synthesis and spectroscopic characterization of low-dimensional carbon materials. Dr. Zhang has published over 170 peer-reviewed journal articles. Currently, he serves as the editor of *Carbon*.

small NANO MICRO

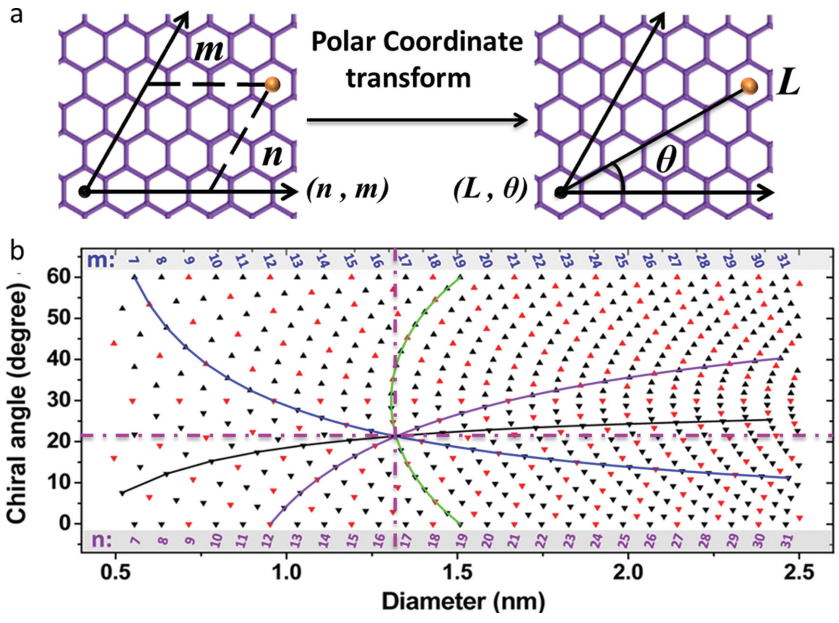

Figure 1. a) Relationship between (n, m) notation and (L, θ) notation. b) The (θ, d) plot for chirality identification. Reproduced with permission.[32] Copyright 2013, ACS.

As 2D graphite can be considered a tube with a diameter $d \to \infty$,[31] E(0) can be regarded as the electronic energy of graphene. By theoretical calculations[33] and experimental measurements from scanning tunneling spectroscopy (STS),[34] the bandgap of a carbon nanotube is found to equal $2\gamma_0 a_{C-C}/d$, where γ_0 = 2.45 eV is the nearest-neighbor overlap integral in graphene. This result proves that the constant of the 1/d term α does not relate to the helix angle θ. However, the constant of the second order term, β, is a function of the helix angle θ. By photoluminescence measurements, the simple model deviates according to $A_i \cos(3\theta)/d^2$, in which A_i is a constant depending on the transition energy level. This is explained by so-called triangle warping effects.[31,35,36] As shown in Figure 2d, in the first Brillouin zone of 2D graphene, the equi-energy contours are circles around the K points, but they change into triangles around the M points. Therefore armchair, or (n,n), tubes distribute equal energy for the transitions in the KΓ and KM directions, while others will have splitting energies depending on their helix angle θ.

2.4.2. Phonon Structure of a SWCNT

Phonons are quantized normal mode vibrations.[31] Similar to the consideration of the SWCNT electronic structure, a folding procedure is generally applied to obtain the phonon structure for SWCNTs from that of a 2D graphene sheet. The 2D graphene sheet has two atoms per unit cell, thus having 6 phonon branches: transverse acoustic (oTA), in-plane transverse acoustic (iTA), longitudinal acoustic (LA), out-of-plane transverse optic (oTO), in-plane transverse optic (iTO), and longitudinal optic (LO). LA, oTA, and iTA are called acoustic branches, while iTO, oTO, and LO are called optic branches. Using a folding procedure similar to that used for the electronic structure, the phonon dispersion relations of a rolled-up SWCNT can be obtained and the corresponding phonon density of states (DOS) can be calculated.

Figure 3 shows the phonon structure of 2D graphene (Figure 3a,b)[37] and a (10, 10) tube (Figure 3c,d).[31] We can find many phonon branches, and the 1D nature of the SWCNTs relative to 2D graphite arises from the quantum confinement of the phonon states. In fact, there are 120 degrees of freedom and 66 distinct phonon branches[2] calculated from the graphene phonon structure using the zone folding procedure.

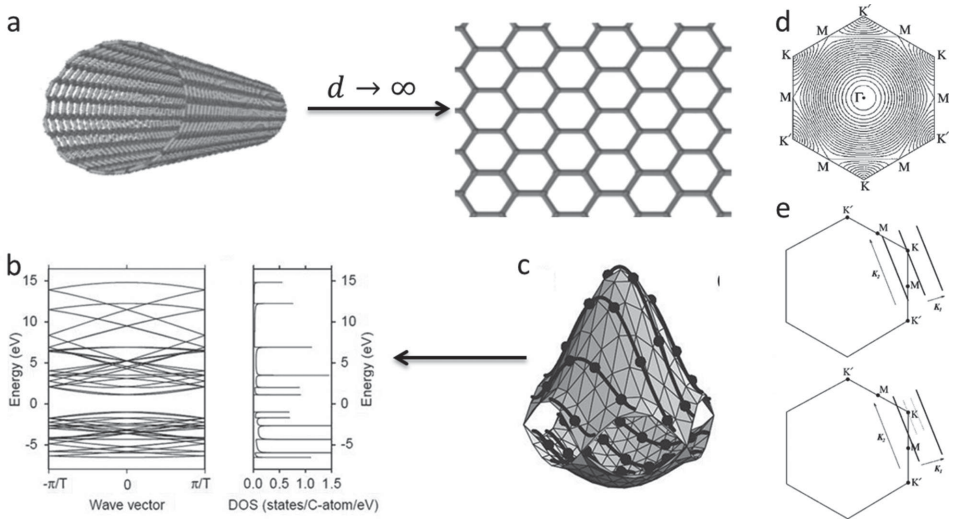

Figure 2. a) Relationship between SWCNTs and graphene. b) Energy states and density of states (DOS) of a SWCNT. c) Electronic structure of graphene and the cutting line of a (4,2) tube. Reproduced with permission.[31] Copyright 2005, Elsevier. d) The first Brillouin zone of 2D graphene with equi-energy contours. e) The wave vector ***k*** for 1D carbon nanotubes in the 2D Brillouin zone of graphite. Reproduced with permission.[35] Copyright 2000, APS.

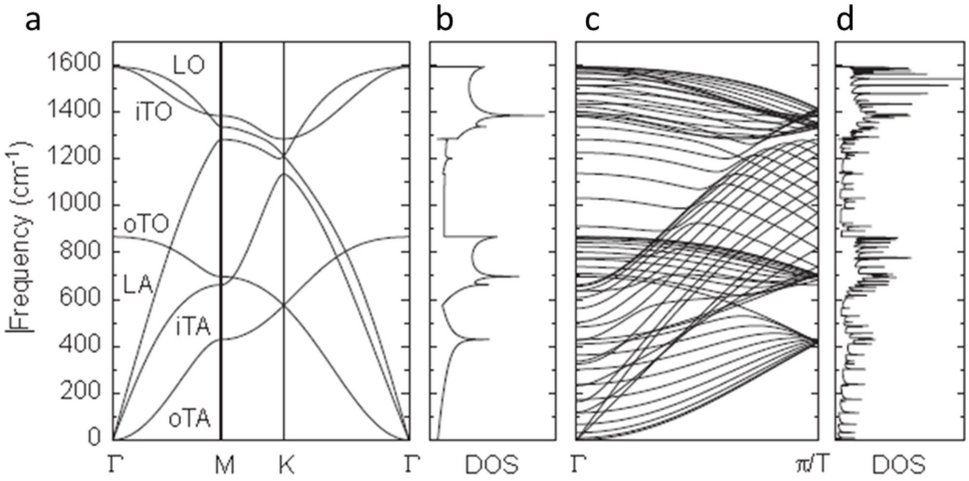

Figure 3. (a) Phonon dispersion of 2D graphite. (b) The phonon DOS for a 2D graphene sheet. (c) The calculated phonon dispersion relations of a (10, 10) tube. (d) The corresponding phonon DOS for a (10,10) nanotube. Reproduced with permission.[31] Copyright 2005, Elsevier.

3. Practical Methods to Determine Diameter

The diameter of a SWCNT can be characterized by several methods. **Figure 4** shows some representative methods. Among these approaches, most of them are imaging techniques, like atomic force microscopy (AFM), scanning tunneling microscopy (STM), high-resolution transmission electron microscope (HRTEM), and selected area electron diffraction (SAED). Spectroscopy techniques, especially Raman spectroscopy, are also used to characterize the diameter in some specific situations. In this section, we mainly focus on the theories and error analysis of these methods.

3.1. Atomic Force Microscopy (AFM)

AFM images microscopic nanostructures by detecting the force between the surface of the structure and the microscope tip. It can be operated under atmospheric pressure, and is compatible with both insulating and conducting substrates. AFM supports a relatively large-scale scan compared to other imaging techniques, which makes it useful for characterizing the diameter distribution of SWCNTs. Random carbon nanotubes,[38] carbon nanotube films[9] on amorphous silicon dioxide, or horizontal arrays on substrates of quartz,[39–41] sapphire,[42–44] or even graphite[45] have been reported. Another advantage is that we can investigate the morphology of the end of a SWCNT on the surface, including cut-off by nanobarriers[46] or catalyst nanoparticles,[41,47] which is helpful to study the mechanism of SWCNT growth. Due to the high vertical resolution of AFM, the accuracy of AFM measurements is 0.2 nm at most.[38]

3.2. Scanning Tunneling Microscopy (STM)

Tunneling currents depend exponentially on the distance between the tip and the surface: distance changes of 0.1 nm may cause one-thousand-fold variations in the current. This endows STM with a very high vertical resolution of 0.01 nm. As shown in Figure 4c and d, we can get an atomic resolution picture by STM.[48,49] Diameters of SWCNTs have also been determined from nanotube images after deconvoluting the tip contribution to the image.[50] Since the apparent height results from the combination of both electronic properties and the topography of the sample, the deconvoluting approach leads to a better measurement than determination from the apparent nanotube height, as the STM experiment measures the local density of states, which rely on properties of substrates and tips. The accuracy of the STM measurement on Au(111) surface can be 0.05 nm at most.[38]

3.3. Transmission Electron Microscopy (TEM)

Transmission electron microscopy is a microscopy technique in which a beam of electrons is transmitted through the specimen. As shown in Figure 4e, the diameter of a SWCNT is measured by the distance of the two minima in the image contrast (or the darkest line in the SWCNT images), which is proved to be relevant.[49] Aberration-corrected HR-TEM (AC-TEM) can also be used to characterize the structure of a SWCNT, as shown in Figure 4f, which makes the resolution higher. The error in the HR-TEM method in determining the diameter of a SWCNT can be less than 0.05 nm.[49]

3.4. Electron Diffraction (ED)

Electron diffraction of an individual SWCNT was first introduced by Qin in 1994,[51] obtained by regarding the tube as a series of molecular helices.[52] The diameter was determined from the equatorial oscillation.[53] The diffraction of SWCNTs can be well described by kinematic diffraction theory. The equatorial oscillation in the Fourier transformation of a helical structure like a SWCNT is a zero-order Bessel function:

$$I_0 \propto \left|J_0(\pi DX)\right|^2 \quad (9)$$

small NANO MICRO

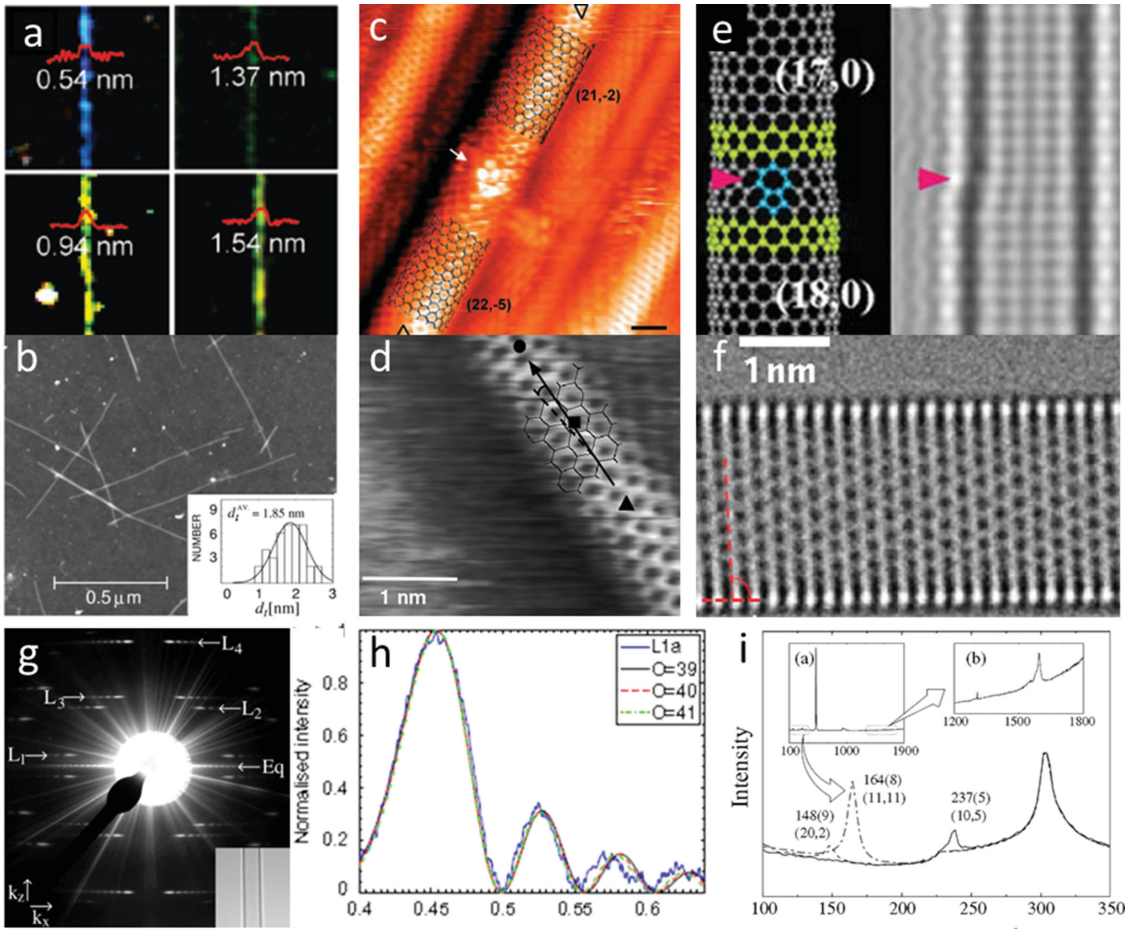

Figure 4. Methods to determine diameter: a,b) AFM. Reproduced with permission.[38,160] Copyright 2001, APS; Copyright 2010, ACS. c,d) STM. Reproduced with permission.[34,87] Copyright 1998, NPG; Copyright 2001, AAAS. e,f) TEM. Reproduced with permission.[49,64] Copyright 2004, NPG; Copyright 2011, NPG. g,h) ED. Reproduced with permission.[65] Copyright 2011, Elsevier. i) Raman spectroscopy. Reproduced with permission.[38] Copyright 2001, APS.

$J_0(x)$ is the zero-order Bessel function, which can be approximated when $\mathbf{x} \gg 0$:

$$J_0(x) \sim \sqrt{\frac{2}{\pi x}} cos\left(\frac{3}{4}x\right) \tag{10}$$

in which x = πDX. R is the reciprocal vector which can be measured from the diffraction pattern, and d is the diameter of the SWCNT. From this equation, we can get the diameter of a SWCNT by fitting the intensity of the equatorial oscillation. The error in ED measurements by nanoarea electron diffraction is estimated to be less than 1% of the diameter of the cylinder, which is smaller than 0.02 nm in most SWCNTs.

3.5. Raman Spectroscopy

Raman spectroscopy can characterize the phonon state of a SWCNT. As mentioned in Section 2.4.2, the phonon structure of a SWCNT can be deduced from 2D graphene. The diameter dependency of the various mode frequencies is expressed by:

$$\omega = \omega_0 + \beta / d_i^n \tag{11}$$

Many experiments have proven that, under a certain energy of the laser, RBM, D,[54] G^-,[55,56] G′,[55] M^+,[57] and M^-[57] modes obey the equation above. Among these, people usually use the RBM peak to measure the diameter. RBM is the 'breathing' vibration mode of a SWCNT, for which all carbon atoms move coherently in the radial direction. RBM is a unique phonon mode appearing only in carbon nanotubes, and its observation in Raman spectra provides direct evidence that a sample contains SWCNTs.[61] RBM is a first-order Raman mode, and its frequency ω_{RBM} is one order of (linearly dependent on) the diameter. Both theoretical[63] and experimental[38,58–62] studies have shown that ω_{RBM} is inversely proportional to the diameter of a SWCNT according to Equation (11), in which n = 1. The relationship between d and ω_{RBM} depends on the substrate and atmosphere of the sample. **Table 1** gives the relationship under different conditions.

The G band is the also a Raman fingerprint of SWCNTs which is commonly observed. In 2D graphene, the G band is the only first-order Raman peak around 1582 cm^{-1}. When wrapped

Table 1. Relationship between the SWCNT diameter and RBM shifts under different conditions.

Relationship	Conditions
$248/d$ [38]	Silicon substrate
$12.5 + 223.5/d$ [58]	Aqueous solution
$27 + 204/d$ [59]	Suspended
$19 + 214/d$ [60]	Silicon substrate
$0.3 + 227/d$ [61]	Super-growth
$228/d$ [62]	Suspended on Si_3N_4/Si Substrate

into a SWCNT, the G band splits into many components, including the higher frequency G^+ and the lower frequency G^-. In SWCNTs, G^- peak shifts with the diameter according to Equation (11), with $\omega_0 = 1591$, $\beta = -47.7$, n = 2 for semiconducting SWCNTs, and $\omega_0 = 1591$, $\beta = -79.5$, n = 2 for metallic SWCNTs. G^+ peak, however, does not vary when the diameter changes; in other words, $\omega_0 = 1591$, $\beta = 0$ in Equation (11).[31]

The error in this method depends on the resolution of the spectrum. If the resolution is 1 cm^{-1}, the accuracy can be less than 0.02 nm.

4. Practical Methods to Determine Helix Angle

The helix angle of a SWCNT can be characterized via several methods. **Figure 5** shows four representative characterizations. STM and HR-TEM can characterize the helix angle easily. SAED can also give us the information on the helix angle independently. A new method, which is based on the interaction between SWCNTs and the graphene lattice, is also introduced. We call it 'graphite-assisted atomic force microscopy'. This graphite-assisted AFM method can be regarded as an ingenious improvement on standard AFM. In this section, we will focus on the theories of these methods, and analyze the error of these methods.

4.1. Scanning Tunneling Microscopy (STM)

As mentioned above, STM measures the local density of states. In STM images, the light part refers to the carbon–carbon bond, while the darker area is the center of the sixcan calculate the helix angle of the SWCNT.

In a perfect SWCNT, a moiré pattern can also be formed by the rolled-up graphene layer. This pattern is clearly visible between two intense dark lines corresponding to the vertical tube walls, as shown in Figure 5e. This delivers information about the helix angle.[64]

Both TEM and STM can give us images at the atomic level, so the error of these methods is mainly caused by the determination of **T** and $\mathbf{a}_1$. The accuracy of HR-TEM is also 0.5°, the same as for STM.

4.2. Electron Diffraction (ED)

In principle, the chiral angle of the SWCNT, helix angle can be measured directly from the diffraction pattern.[65] Because of the structure of a rolled-up graphene layer, the diffraction pattern from a SWCNT can be simply understood by

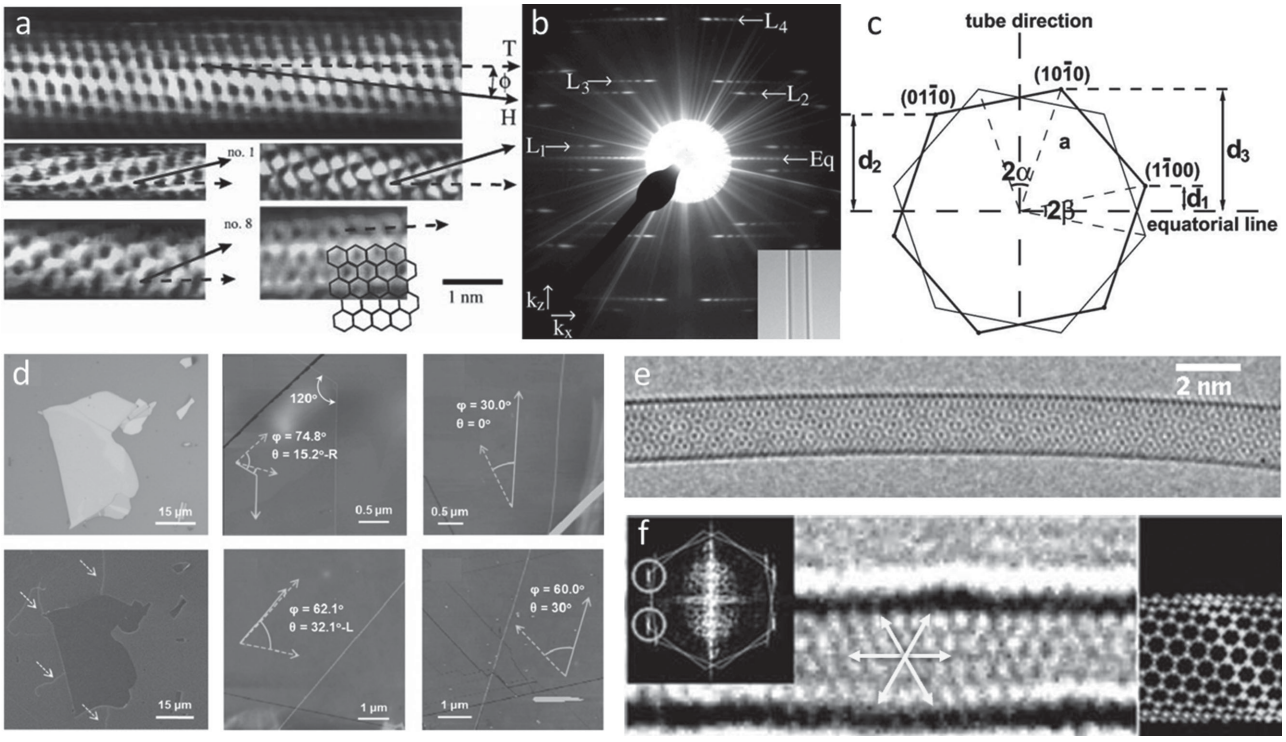

Figure 5. Methods to determine helix angle. a) STM. Reproduced with permission.[71] Copyright 1998, NPG. b,c) ED. Reproduced with permission.[53,65] Copyright 2003, AIP; Copyright 2011, Elsevier. d) Graphite-assisted AFM. Reproduced with permission.[32] Copyright 2013, ACS. e,f) TEM. Reproduced with permission.[49,64] Copyright 2004, NPG; Copyright 2011 NPG.

small NANO MICRO

considering diffraction from two parallel sheets of graphene. When the incident electron beam is normal to the tube axis and sequentially passes through the two graphene sheets (corresponding to the 'top' and 'bottom' walls of the carbon nanotube), as shown in Figure 5c, the resultant diffraction pattern is the sum of the diffractions from each graphene sheet. If the graphene sheets rotate with respect to one another about the axis normal to the plane of the sheets, the two diffraction patterns will also rotate by the same angle.

Though measuring the angle between two diffraction patterns may cause a bigger error, we can calculate the angle from the following equation:

$$\theta = arctan\left(\frac{1}{\sqrt{3}}\cdot\frac{d_2-d_1}{d_3}\right) = arctan\left(\frac{1}{\sqrt{3}}\cdot\frac{2d_2-d_3}{d_3}\right) \quad (12)$$

in which d_1, d_2, and d_3 are the distances between the diffraction lines and the equatorial oscillation.

The error in ED measurements by nanoarea electron diffraction is estimated to be less than 0.2°.

4.3. Graphite-Assisted Atomic Force Microscopy

As mentioned above, AFM can operate under atmospheric pressure and is suitable for both insulators and conducting substrates. However, normal AFM could not realize atomic resolution. Over these years, an improvement in AFM called the Q-plus technique, has been shown to make up for this disadvantage, and both covalent bonds[66] and hydrogen bonds[67] can be observed. The surface topography of nano-graphene has also been imaged by this technique. However, this technique has a very small scanning area, which limits its application.

To overcome the limitations of AFM, our group developed a method to characterize the helix angle of a SWCNT with the help of the graphene lattice. As we all know, in the case of anisotropic surface-mediated growth of SWCNT arrays, the orientation of SWCNTs is determined by the surface lattice[68] or the atomic terraces[69] on the high-anisotropy substrates. Although the graphene lattice has a symmetry of D_{6h}, it can also display a surface-mediated effect for SWCNT growth. Furthermore, because of the π–π stacking effect between SWCNT and the graphene substrate, the orientations of SWCNTs with different helix angles have evident differences. As shown in Figure 5d, SWCNTs with different helix angles show different included angles, referring to the channel (the darker line) on graphite. The darker lines are the etched trenches on a graphite surface by the Fe catalyst, which is proven to be the zigzag edge. From the AFM images, it is easy to obtain the angle ϕ relating to the helix angle θ:

$$\theta = 30^\circ - \phi 0^\circ < \phi mod 60^\circ < 30^\circ \quad (13)$$

$$\theta = 90^\circ - \phi 30^\circ < \phi mod 60^\circ < 60^\circ \quad (14)$$

This method can give us information about helix angles using AFM. The error of the method depends on the trend of the graphene, which can realize an accuracy of 1°, approximately.

5. Practical Methods to Determine the Electronic Energy State

As shown in **Figure 6**, several methods have been developed to characterize the electronic structure of SWCNTs. Scanning tunneling spectroscopy (STS) measures the local DOS, which can describe the electronic structure by dI/dV bias voltage-dependent curves. Photoluminescence (PL) methods can get the E_{11} and E_{22} electronic states at the same time. Resonant Raman spectra and resonant Rayleigh spectra, based on the resonant scattering phenomenon, can be used to measure the E_{ii} of a SWCNT. The error of the spectroscopy method mostly depends on the resolution of the spectroscopy and the function we choose to fit the peak. For a perfect peak type, the accuracy could be $\pm 1\ cm^{-1}$. The error for spectroscopy techniques will not be discussed in the following section.

5.1. Scanning Tunneling Spectroscopy (STS)

In scanning tunneling spectroscopy, the normalized conductance, dI/dV, which has been shown to provide a good measure of the major features in the local density of electronic states (LDOS) for metals and semiconductors,[70] was calculated from digital I-V data using standard methods.[50,71] As shown in Figure 6a,[34] the I-V data recorded with this atomic-resolution image (Figure 6a inset) shows the same behavior as a semiconductor: The tunneling current is relatively small when the bias voltage (V) is in the range of –300 mV to 400 mV, but increases sharply when when $|\mathbf{V}|$ increases further. The calculated dI/dV shows sharp increases at –325 mV and 425 mV that correspond to the conduction and valence band edges in the LDOS, and thus we assign a bandgap of 750 meV.

This method has a significant error of 50–100 meV,[71] which makes it difficult to become a credible method in measuring electronic structures. Nevertheless, the I-V data can be an important reference to choose the correct chiral index among several possibilities. For example, Figure 6a shows a SWCNT with possible chiral indices of (14, –3) or (15, –3). The I-V curve shows strong evidence of a semiconducting feature. As mentioned in Section 2.3, (14, –3) is a semiconducting SWCNT while (15, –3) is a metallic one at room temperature, so the real chiral index should be (14, –3).

5.2. Photoluminescence (PL) Spectroscopy

In photoluminescence excitation (PLE) spectroscopy, the PL intensity of the sample is measured with respect to both excitation and emission wavelengths. After being induced by absorbing photons with a certain energy, the excitons can release the excess energy via different decay channels. Since there is a certain DOS near the Fermi level, metallic SWCNTs will lose the excess energy of the excitons by rapid nonradiative decay, thus no PL will be observed. For semiconducting

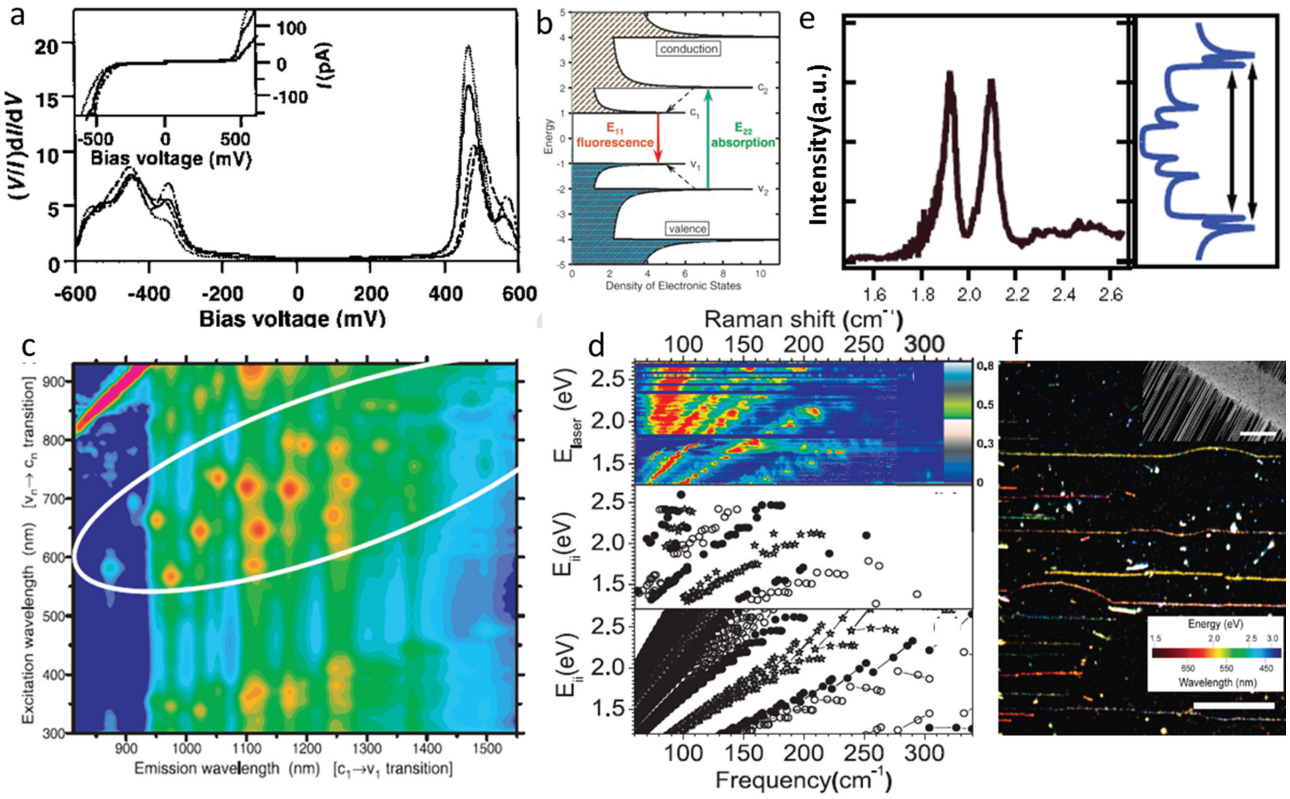

Figure 6. Methods to determine electronic energy states: a) STS. Reproduced with permission.[34] Copyright 1998, NPG. b,c) PL spectroscopy. Reproduced with permission.[58] Copyright 2002, AAAS. d) Resonant Raman spectroscopy. Reproduced with permission.[147] Copyright 2008, Wiley-VCH. e,f) Resonant Rayleigh spectroscopy. Reproduced with permission.[74,160] Copyright 2004, AAAS. Copyright 2010, ACS.

SWCNTs, however, there is a bandgap, so the excitons will relax to the lowest-lying excitonic states, and then recombine by radiative PL with the photon energy corresponding to the lowest-lying excitonic state.

In most cases electronic transitions are only allowed between electronic valence and conduction bands with the same symmetry, and the corresponding electronic transitions can be labeled as E_{ii}. The subscript numerals refer to the corresponding van Hoff Singularities (vHSs) in the valence and conduction bands, respectively, counting away from the Fermi level. Figure 6b shows the basic PL process for a semiconducting SWCNT.[58] Figure 6c[58] shows the PL characterization of suspended SWCNTs dispersed in D_2O. The white oval marks a region of special interest that contains discrete peaks. Within the circled region, many spectral features that overlap in simple emission or absorption spectra are clearly separated in the two-dimensional excitation–emission spectrum. The excitation energy of photons in the circled region refers to the E_{22} transition of the SWCNT, while the emission energy refers to E_{11} state. The other peaks under the white circle are the signals from the SWCNTs which are excited to higher E_{ii} energy states, like E_{33} or E_{44}.

5.3. Resonant Raman Spectroscopy

The first-order Raman intensity as a function of phonon energy, $\hbar\omega$, and of the incident laser energy, E_L is calculated by the following equation:[72]

$$I(\omega, E_L) = C\left(\frac{E_a}{E_j}\right)[n(q,\mu)+1]$$

$$\sum_j \left| \sum_a \frac{M^d(k-q,jb)\,M^{ep}(q,ba)\,M^d(k,aj)}{\Delta E_{aj}\left(\Delta E_{aj} - h\omega\right)} \right|^2 \qquad (15)$$

where C is a constant depending on (n, m), while $n(q,\mu)$ is the number of phonons. $\Delta E_{aj} \equiv E_L - (E_a - E_j) - i\gamma$, in which j, a, and b denote the initial state, excited state, and the scattered state of an electron, respectively. γ denotes the broadening factor of the resonance event. The matrices $M^d(k-q,jb), M^{ep}(q,ba)$, and $M^d(k,aj)$ stand for the electric dipole interaction in photon absorption, the electron–phonon interaction in phonon scattering, and the electric dipole interaction in photon emission, respectively. We can simplify Equation (15) for a transition with a specific transition energy E_{ii}:

$$\mathrm{I} \propto \left| \frac{M}{(E_L - E_{ii} - i\gamma)(E_L - E_{ii} - h\omega - i\gamma)} \right|^2$$

$$= \frac{|M|^2}{\left[(E_L - E_{ii})^2 + \gamma^2\right]\left[(E_L - E_{ii} - h\omega)^2 + \gamma^2\right]} \qquad (16)$$

From Equation (16), we can see that for either $E_L = E_{ii}$ or $E_L = E_{ii} + h\omega$, the resonance is maximized. The former is

NANO MICRO small

called the incident resonance condition, while the latter is called the scattered resonance condition. When E_L lies very close to E_{ii}, in another words, when E_L is within the resonance window of E_{ii}, the signals will be significantly enhanced: even Raman signals of individual SWCNTs can be observed. The resonance window of RBM is commonly assumed to be about ±0.1 eV. Thus, the environmental effects can also affect the resonance window width of SWCNTs.

As shown in Figure 6d,[73] resonance Raman spectra of 125 SWCNTs were used to generate a 2D plot giving the Raman intensity as a function of the laser excitation energy and radial breathing mode frequency (ω_{RBM}). The graph in the bottom is a Kataura plot for super-growth SWCNTs, which is proven to be identical with the experimental results.

The electronic transition energy E_{ii} of SWCNTs can also be speculated by the anti-Stokes/Stokes resonant Raman intensity ratio, which follows the following relationship:[31]

$$I(E_{ii}) \propto \left| \frac{Mg(E)}{(E_L - E_{ii} - i_r)(E_l \pm E_{ph} - E_{ii} - i_r)} \right|^2 \quad (17)$$

where E_l, E_{ii}, and E_{ph} represent the laser energy, the electronic transition energy of SWCNTs, and the phonon energy, respectively. Γ_r is associated with the lifetime of electronic states in the resonance process.

5.4. Resonant Rayleigh Spectroscopy

Resonant Rayleigh spectroscopy is another technique depending on the resonance between the incident laser energy and the electronic state. Rayleigh scattering is an ubiquitous process of elastic light scattering from a small, polarizable object.[74] Rayleigh scattering occurs whether or not the sample luminesces, and it does not require the incident light to couple with the vibrations of the system, which makes it intrinsically stronger than Raman scattering.

Like Raman enhancements caused by the resonance phenomenon mentioned in Section 5.3, resonant Rayleigh spectra can also measure the E_{ii} state. As shown in Figure 6e,[74] it can provide spectrographic information about the system through the scattering resonance enhancement when the photon energy matches that of an electronic transition. When implemented with a bright white-light source, the technique offers sufficient versatility and speed to probe spatially localized regions along an individual nanotube. Figure 6f shows a mapping graph of a SWCNT array, from which we can see SWCNTs in different colors, which refer to different resonant Rayleigh scattering wavelengths.

6. Practical Examples

As mentioned in Section 2.2, two independent parameters are necessary to determine the chiral index of a SWCNT. In Sections 3, 4 and 5, we have reviewed routes to measure three different parameters, including diameter, helix angle, and electronic state, which are independent from each other. Any two out of these three parameters can uniquely determine the (n, m) of a SWCNT. Theoretically, arbitrary combinations of characterization methods for the derivation of different parameters can be used. For example, we can choose STM to measure the diameter, and SAED to characterize the helix angle to determine (n, m) indices. However, if we consider simplicity, some combinations are better than others. **Table 2** highlights the combinations which are widely used to characterize the chiral indices of SWCNTs.

From the table we can see that, among the methods above, STM, HR-TEM, SAED, and Raman spectroscopy (RS) techniques can realize the determination of the chiral index independently. Resonant Rayleigh spectroscopy can only get the information of electronic energy, so it needs the diameter or helix angle determination with the cooperation of other methods. AFM has the same problem, before the improvement via graphite-assisted AFM. In the following sections, we will introduce more details about these methods, including their instruments, sample preparation and data analysis. A range of applications will also be discussed in each section. Furthermore, two special methods will be introduced in the last section.

6.1. Chiral Index Determined by STM

As mentioned above, STM requires a conductive substrate. Hence, to characterize the diameter of a SWCNT, samples are mostly prepared by spin coating nanotube suspensions of dichloroethane on Au(111) surfaces.[34,71] Before inserted into an STM, samples should be imaged by AFM to ensure the SWCNTs are dispersed on the substrate. A 1 μm separation between SWCNTs should be appropriate for STM measurements. STM imaging studies are carried out at a low temperature and under ultrahigh vacuum (UHV).[75] Both electrochemically etched W tips[34] or scissor-cut Pt–Ir tips[71] can be used. Topographic images are obtained by recording the tip height at constant tunneling current.

STS measurements are made by averaging several current vs. voltage (I-V) curves at specified locations on atomically resolved SWCNTs. To ensure the reliability of these measurements, a routine check ensures that clean areas of the Au(111) substrate exhibit characteristic metallic I-V curves

Table 2. Combinations widely used to characterize the chiral indices of SWCNTs based on a) the (d, θ) method, b) the (θ, E_{ii}) method, and c) the (d, E_{ii}) method.

E_{ii}-d	AFM	TEM	STM	ED	RS
PL					☆
STM					
RR_aS					☆
RR_eS	☆				☆

θ-d	AFM	TEM	STM	ED	RS[1]
TEM		☆			
STM			☆		
ED				☆	
GA[4]	☆				☆

E_{ii}-θ	TEM	STM	ED	GA
PL				
STM				
RR_aS[2]				☆
RR_eS[3]				

1:Raman spectroscopy
2:Resonant Raman spectroscopy
3:Resonant Rayleigh spectroscopy
4:Graphite-assisted AFM

and the expected 2D surface state[76] of this material. Typically the I-V curves of 6–8 distinct locations are measured. The normalized conductance, dI/dV, is calculated from digital I-V data using standard methods.[34]

As shown in Sections 3.2 and 4.1, we can get the diameter and the helix angle of a SWCNT. For example, Figure 5a shows an image of a chiral SWCNT. From the image we can get the diameter d = 1.3 nm and the angle $\phi = 7°$. By Equation (12), we can calculate the helix angle $\theta = 30° - \phi = 23°$, which corresponds to the (11, 7) type. Sometimes, other chiral indices are near the (d, θ) measurement, and then determination of the electric properties by STS is indispensable.

STM and STS methods can easily get the structure of an observed SWCNT under the microscope. However, if we want to characterize a given SWCNT, we may need some special procedure, like site-directed transfer. Nanodevices can help to solve the problem caused by insulating substrates in some circumstances. For example, when a SWCNT is located on a small piece of graphite and the graphite is on an insulating substrate, the process can help to get the STM image of the SWCNT.[45] After covering the sample with a thin film of PMMA, Cr/Au (5/75 nm) electrodes around the edge of the graphite are patterned via a standard electron beam lithography (EBL) process. The PMMA film is then carefully removed. The electrode is linked to the Au wire by pressure welding. After a necessary annealing process,[77] the nanodevice can be used for characterization with STM.

STM can also give us a chirality distribution if a sufficient amount of tubes are characterized. For example, Lieber and co-workers counted the chirality distribution of purified nanotubes, discovering a richness of structures favoring helicities closer to the zigzag (n, 0) direction rather than the armchair (n, n) direction.[78] Selective chemical etching was also analyzed in the same work.

With STM techniques, we can not only characterize individual perfect SWCNTs, but also the interactions and lattice-matched structures in SWCNT bundles.[79–81] Defects in bent regions,[82–84] ends,[85,86] and junctions[87] can also be characterized from their atomic-scale images. However, defects are usually not clearly visible in these regions because the local DOS, which are measured in the STM experiment, do not necessarily reflect the atom positions.

Though STM can get an atomic-resolution image, it requires a long data acquisition time, and the scanning area is relatively small. The complication in sample preparation also limits its application as a general characterization method, especially for as-grown SWCNTs on an insulating surface. In addition, this method can only characterize the outside layer of a carbon nanotube, making it unsuitable for multiwalled carbon nanotube characterization.

6.2. Chiral Index Determined by TEM

Unlike STM, TEM requires a suspended sample. Many methods can be used to prepare samples. The simplest is to place nanotubes on a microscope specimen grid by drying a drop of the suspension on the grid.[1] Catalysts can also be loaded onto the TEM grid, and then SWCNT films can be grown there during TEM characterization to realize an in-situ investigation of the SWCNT growth process.[88,89] However, these methods have poor controllability, for the position and direction are impossible to control. To get controllably orientated SWCNT arrays across the grid, in-situ gas flow-directied growth can be used for sample preparation.[62,90] Carbon nanotubes can be grown by chemical vapor deposition (CVD) across commercially available perforated silicon oxide[90] or Si_3N_4/Si substrates using standard photolithography and wet-etching processes.[91] Then as-grown SWCNTs can be observed through grids on the substrates. Horizontal arrays can be transferred onto the grid by commonly used transfer procedures.

In Sections 3.3 and 4.2, we discussed methods to determine the chiral index of a SWCNT by (d, θ) measurements. Though the basic theories of STM and HR-TEM are different, the procedures of analysis are basically the same, for both of them rely on atomic-resolution images in perfectly structured tubes.

Using HR-TEM, we can also study the defects and junctions in SWCNTs. Unlike the description of the local DOS in STM, HR-TEM directly images the position of the atom, which makes it easy to investigate defects. Typical stable graphene defects, such as pentagon–heptagon pairs,[92] vacancies,[93–95] and adatoms,[96,97] have also been discovered in SWCNTs using HR-TEM.[49,98–100] Among all kinds of topological defects, pentagon-heptagon pairs, or '5–7 defects', have received the most attention. In the case of SWCNTs, 5–7 defects are considered to induce a local deformation and diameter discontinuity, that is, a local change in the chiral index.[101,102] These 5–7 defects are also predicted to exist in the intramolecular junctions shown using STM,[87] but have not been observed directly. However, with TEM, atomic-resolution images of 5–7 defects can be acquired. These defects, at first, were considered to be immobile at ambient temperatures.[103,104] However, at 2273 K, the defects were found to move and accumulate near the kink of a SWCNT.[98]

More things can be done by determining the real positions of carbon atoms and the centers of the rings. Warner and co-workers used HR-TEM to resolve strain in SWCNTs at the atomic level.[64] They deposited SWCNTs from a solution of 1,2-dichloroethane onto a lacey carbon-coated TEM grid. By this approach, isolated nanotubes were suspended across free space, thereby enabling a substrate-free image. The bending observed in the SWCNTs was a direct consequence of drying from the solvent and fixing onto the lacey grid. By comparing simulated and experimental HR-TEM images of a (28,0) tube, they got a 2D displacement map. By analyzing the displacement, they showed the existence of a dominant nonuniform shear strain that varied along the SWCNT axis. This work highlights the complex atomistic strain behavior of beam-bending mechanics in highly anisotropic SWCNTs.

TEM has the same limits as STM: a long data acquisition time and small scanning area. Furthermore, the small atomic mass of carbon renders it easily damaged by the electron beam when examined using HR-TEM.[105,106] The advancement of aberration-corrected HR-TEM now permits angstrom-level resolution at a low accelerating voltage

small NANO MICRO

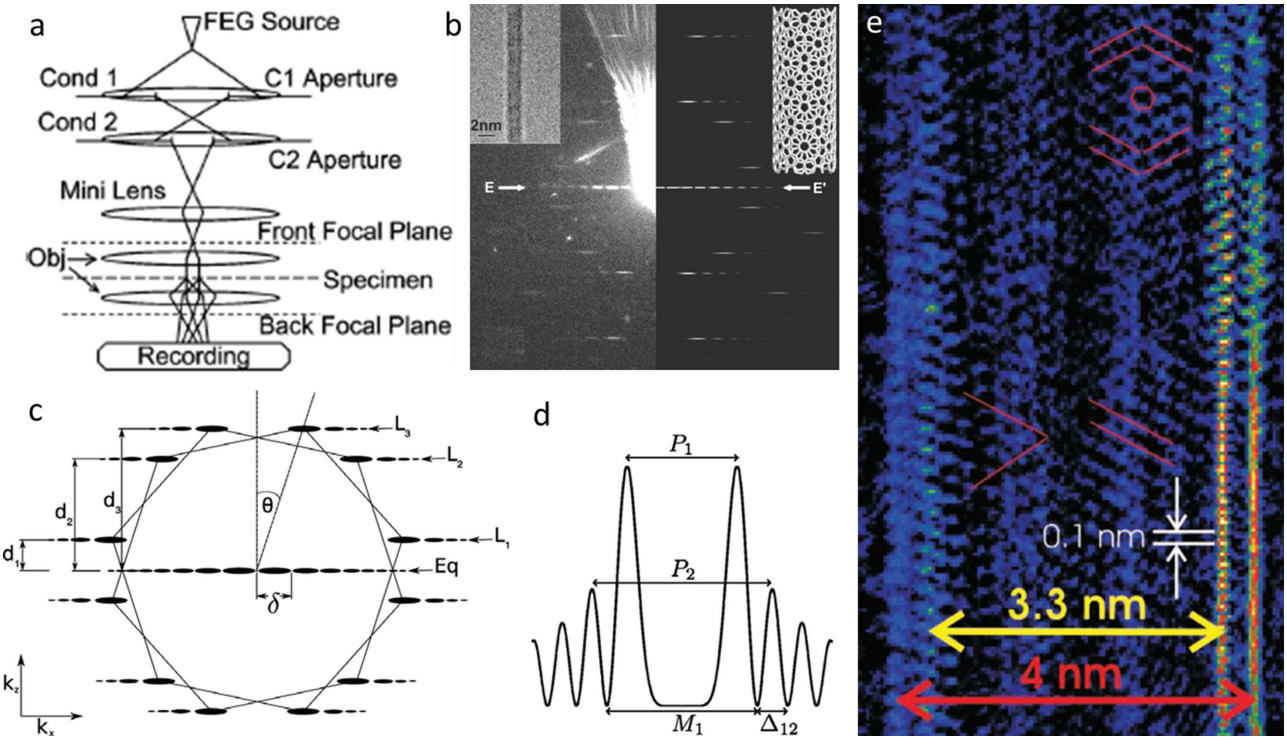

Figure 7. a) Schematic diagram of nanoarea electron diffraction. b) Comparison of diffraction patterns between experimental (left) and theoretical (right) results. Reproduced with permission.[53] Copyright 2003, AIP. c) A schematic depiction of the diffraction pattern obtained from a SWCNT. d) The theoretical form of the radial intensity distribution of one of the layer lines. Reproduced with permission.[65] Copyright 2011, Elsevier. e) A section of the reconstructed DWCNT image at 1 Å resolution. Reproduced with permission.[125] Copyright 2003, AAAS.

of 80 kV, and thus enables the carbon atoms in sp^2 graphitic nanomaterials such as graphene and SWCNTs to be directly imaged.[64,107] However, some SWCNTs, especially those with small diameters (1 nm), are also damaged under these conditions.

6.3. Chiral Index Determined by ED

Electron diffraction, in principle, can unambiguously determine both the chirality and diameter of tubes, and thus it has been widely used for characterizing the chiral index of a SWCNT since 1993.[1,108,109] However, conventional diffraction patterns of individual SWCNTs are too blurry, making them difficult to identify, as the electron diffraction from a SWCNT can be extremely weak and often below the sensitivity of the equipment. In 2003, Gao and co-workers reported an improved quantitative structural determination of SWCNTs by nanoarea electron diffraction in a field-emission electron microscope, recorded with image plates.[53] **Figure 7**a shows the schematic diagram of nanoarea electron diffraction. The electron beam is focused to the focal plane of the objective prefield, and forms a parallel beam illumination on the sample. The size of the parallel probe is determined by the condenser aperture. For an aperture of 10 mm in diameter, the probe diameter is ~50 nm, which is much smaller than for conventional SAED, and does not suffer from aberration-induced image shifts.[110] Nanoarea electron diffraction also provides a higher beam intensity than SAED, with the probe current intensity of 10^5 e/s nm^2. Both the small area and the high beam intensity are important for the investigation of SWCNTs because of the small scattering cross-section of carbon, and the requirement of a straight tube for electron diffraction. The sample preparation for ED is the same as for HR-TEM, discussed in Section 6.2.

The diffraction pattern of a SWCNT often has two features, which are shown in Figure 7c: a relatively strong equatorial oscillation (Eq), which is perpendicular to the direction of the tube, and some very weak diffraction lines from the graphite sheet (L_1~L_3), which are elongated in the direction normal to the tube direction.[111] Figure 7d shows the theoretical form of the radial intensity distribution of the layer lines. As mentioned in Sections 3.4 and 4.3, we can get information about the diameter from the Eq simulation, and about the helix angle from the distance between diffraction lines L_1~L_3 and Eq(d_1~d_3). More information can be obtained from the diffraction pattern.[52,112] For example, the ratio between the two chiral indices, m/n, can be calculated directly from d_i:

$$\frac{m}{n} = \frac{d_2 - d_1}{d_2 + 2d_1} = \frac{d_3 - 2d_2}{d_3 + d_2} = \frac{2d_2 - d_3}{2d_3 - d_2} \quad (18)$$

More theoretical analyses for SWCNTs are given by Qin.[51]

Performing diffraction studies within a transmission electron microscope has become arguably by far the most powerful technique for the accurate determination of the chirality of individual SWCNTs,[65] and ED methods are widely used to identify certain SWCNTs.[113–115] For example, Jourdain and co-workers observed the atomic structure of ultra-long

carbon nanotubes along the nanotube length via electron diffraction.[116] This work provided direct evidence that the atomic structure is conserved along a SWCNT, as compared to different indirect methods which indicated structural changes.[21,26,27,117]

Deformations can also be studied via ED. Any external forces can lead to the deformation of a tube, so diffraction can alter the structure and lead to mis-assignment of the chiral indices. Elliptical deformation,[118,119] asymmetric deformation,[120,121] and torsional twisting[122] have been reported.

As well as being used for chirality measurements of SWCNTs, ED can also measure the structure of multiwalled carbon nanotubes (MWCNTs),[121,123] which is regarded as a challenge for STM or HR-TEM methods. As shown in Figure 7e, Zuo and co-workers got an image of a double-walled carbon nanotube using nanoarea electronic diffraction.[124] The missing phase could be retrieved ab initio from the diffraction intensities[125] by iterative measurements. With the analysis of the diffraction pattern, a double-walled carbon nanotube (DWCNT) was found to be a (26,24) tube nested inside a (35,25) tube, with an inter-wall spacing of 0.7 nm. The complex patterns in the projection are due to the combination of accidental coincidence and moiré fringes. The application of the procedure is demonstrated as an example for an eleven-shell carbon nanotube whose chiral indices of each and every shell were determined unambiguously.[126] Ropes containing multiple tubes have also been investigated.[127]

With similar equipment to TEM, ED technology shares the same limitations as HR-TEM, mentioned in Section 6.3. Though the acceleration voltage can be as high as 200 kV,[53] it is easy to damage the sample. In addition, this method cannot distinguish the handedness, for example, (7, 2)-R and (2, 7)-L tubes.

6.4. Chiral Index Determined by Graphite-Assisted AFM

As mentioned above, our group have developed a new method, which is based on AFM, to characterize the chiral indices of SWCNTs.[32] The van der Waals interactions between two graphite layers is strongest when their stacking configuration is AB. Similarly, the maximum interaction between a SWCNT and graphite can be achieved if their interface has a similar AB stacking geometry.[128,129] Calculations have been done to ensure the analysis above.[45] Theoretical calculations based on the registry-dependent interlayer potential[130] were performed to explore the interfacial energies between SWCNTs and the graphite surface. Both the aligned SWCNTs and the graphite substrate are considered to be rigid and only a single rigid graphene layer was used to model the graphite, because the interaction between the SWCNT and other graphene layers is negligible. In agreement with previous analyses, the results show that (10, 0), (7, 2)-R, (2, 7)-L and (5, 5) SWCNTs have a minimum energy at torsion angles of $0° + i \times 60°$, $12.2° + i \times 60°$, $47.8° + i \times 60°$, and $30° + i \times 60°$, respectively. To investigate the helix angle selectivity of SWCNTs experimentally, the kite-flying process was used to grow SWCNTs on a graphite surface.[130] Helix angles of the as-grown SWCNTs can be calculated using Equations (14) and (15), depending on the included angle between the SWCNT and the trend of graphite. The diameter can also be measured using AFM by calculating the height difference in the z axis. Then the chiral index can be determined via a d-θ plot, which is shown in Figure 1c. Raman spectra can also assist in measuring the diameter or the electronic state, but this is not as direct as AFM.

This method provides a new route to characterize the diameter of a SWCNT. However, application is relatively narrow provisionally, for it is difficult to utilize van der Waals' forces between SWCNTs and graphite.

6.5. Chiral Index Determined by PL

PL techniques can determine the chiral indices by probing the electronic structure. Both SWCNTs dispersed in solution and individual SWCNTs over trenches can be characterized by this method.

6.5.1. PL Characterization of SWCNTs in Solution

Unlike the methods mentioned above, the PL method can characterize a large amount of samples, such as powder-like SWCNTs, at once. SWCNTs should be well dispersed before this characterization step,[131] for bundling can perturb the electronic structure of the tubes and thus influence the PL emission.[132–134] Moreover, additional points may appear in the PLE map due to exciton energy transfer between the tubes inside the bundle. In 2002, O'Connell and co-workers developed a method to disperse SWCNTs using sodium dodecyl sulfate (SDS):[131] SWCNTs produced from a high-pressure CO reactor (the HiPco process) were dispersed in aqueous SDS surfactant (1 wt%) by high-shear mixing for 1 h. The resulting dispersion was then treated in a cup-horn sonicator for 10 min. After sonication, samples were centrifuged immediately at 122 000*g* for 4 h. The supernatant was then carefully decanted, giving micelle-suspended nanotube solutions at a typical concentration of 20 to 25 mg/L. After performing spectroscopy measurements using a commercial spectrofluorimeter, measurements were corrected for instrumental variations in excitation intensity and detection sensitivity to give a contour plot,[58] as shown in Figure 6c. The excitation-dependant ν_{11}/ν_{22} diagram was then calculated, shown in **Figure 8**a. Figure 8b displays the computed findings from an extended tight-binding model calculation on SWCNTs.[135] By comparing these two diagrams, we can easily get the chiral indices of these points. Reference [58] also shows the table of spectral data and assignments for the SWCNTs, which can help to determine the chiral index. This method can also analyze the content of different SWCNTs semi-quantitatively, for the quantum yields vary for the (n, m) indices,[136,137] as shown in Figure 8c. However, the quantum yield also depends on the length and the environment of the tubes,[138,139] which limits the accuracy of the quantitative analysis.

Based on the electronic transitions of SWCNTs, absorption spectra can also determine the electronic state, as

small NANO MICRO

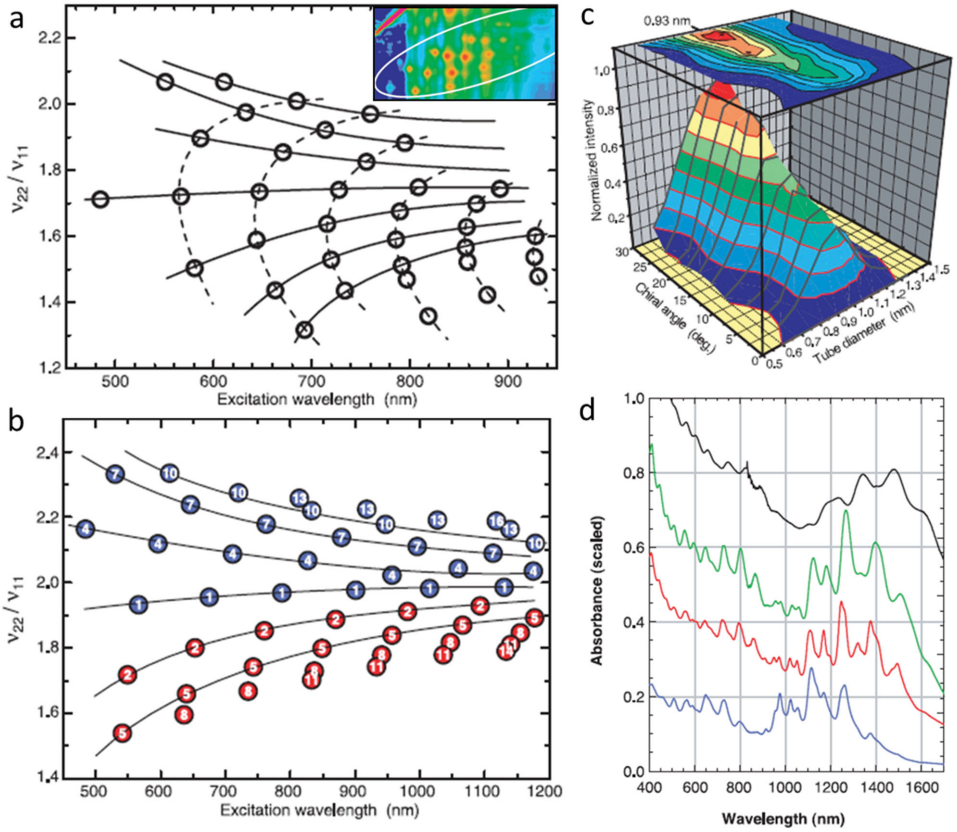

Figure 8. a) The excitation-depend v_{11}/v_{22} diagram. b) Computed findings from an extended tight-binding model calculation on SWCNTs. c) The quantum yields varying for the (n, m) indices. Reproduced with permission.[58] Copyright 2002, AAAS. d) Absorption spectra of SWCNT solutions. Reproduced with permission.[131] Copyright 2002, AAAS.

shown in Figure 8d. This method can only characterize the E_{ii} state of semiconducting SWCNTs. Meanwhile, it is impossible to figure out the corresponding E_{11} and E_{22} of each SWCNT, which limits its application to characterize the chirality. Absorption spectra are mostly used to analyze the content of tubes with different electronic properties.[140–142]

6.5.2. PL Characterization of Individual SWCNTs

In 2003, Hartschuh and co-workers measured the electronic structure of individual SWCNTs using single-molecule photoluminescence spectroscopy.[143] Spatially isolated individual SWCNTs were achieved by spin-coating ~75 μL of the SWCNT suspension onto a glass coverslip. The spin-coating procedure results in well-dispersed individual SWCNTs on a thin surfactant layer. Laser excitation at 633 nm ensured a spectral isolation of all Raman signals, which occur between 633 and 770 nm, from the fluorescence signals above 850 nm. They got several single fluorescence bands with smooth line shapes, which can be used to analyze the electronic state of E_{11}. Raman spectra are used to provide more reliable (n, m) assignments based on E_{11} and diameter.[144,145] Although the substrate can greatly reduce or quench PL, the effect can be eliminated if the SWCNTs are across trenches etched into the substrate.

The PL method, however, also has limitations regarding the characterization of chiral indices of SWCNTs. Firstly, PL is only applicable for semiconducting SWCNTs, because of the continuous DOS at the Fermi level of metallic SWCNTs which will quench PL. Furthermore, the most commonly used InGaAs detector is only applicable for emission from tubes with diameter less than 1.3 nm. Longer wavelength detectors such as the HgCdTe detector[146] may solve this problem. The influence from the substrates or surfactants should also be considered during analysis of the electronic structure.

6.6. Chiral Index Determined by Resonant Raman Spectroscopy

Resonant Raman spectroscopy can characterize the chiral index of a SWCNT individually. Raman experiments can be done at room temperature and under ambient pressure, therefore not requiring complicated preparation processes. For powder samples, the preparation procedure is similar to that for the PL method. For as-grown, aligned SWCNTs on a crystal surface, however, some substrates (like quartz) may influence the RBM signal of the SWCNTs,[136] thus it is better to transfer the tubes onto a Si-SiO_2 substrate. With a tunable laser as the excitation source, we can get information about both E_{ii} and ω_{RBM} simultaneously, and the (n, m) indices can be assigned by referring to the Kataura plot, as shown in Figure 6d.[147] By using two triple-monochromator Raman spectrometers and a total of 125 different excitation laser

lines covering 1.26 eV to 2.71 eV, Araujo and co-workers got an almost continuous 3D Raman excitation spectrum. Each RBM peak in the spectrum corresponds to a SWCNT with E_{ii} in resonance with the corresponding E_L. The diameters of the SWCNTs are given by $\omega_{RBM} = 227/d$. Based on the Kataura plot, we can assign the (n, m) indices with certain (d, E_{ii}). Since the ω_{RBM}–d relation varies under different conditions (as shown in Table 1), a suitable ω_{RBM}–d calibration curve for the specific sample is required.

Most Raman equipment, however, does not have a tunable laser. If the generating laser carries out only a few laser lines, not all tubes can be resonant. With a single laser line, the E_{ii} value can be usually estimated within about ±0.1 eV according to the resonance window width. By using the experimental ω_{RBM} combined with the reported ω_{RBM}–d relation in Table 1, d can be calculated within an average error of ±0.02 nm.[148] The uncertainties in both E_{ii} and d provide a region of possible (n, m) locations with one or more points. To assign the accurate (n, m) from several candidates, another resonant laser is need. If RBM signals under both lasers are observed, the calculated d range from ω_{RBM} and the resonance window of both lasers may probably locate the tube to a specific (n, m). Although the probability of a SWCNT being distinguishable in resonance with two or more laser lines is relatively low, resonant Raman spectra created with a few laser lines can only measure SWCNTs with small diameters with satisfactory accuracy, for the differences between 1/d are large enough to be distinguished by micro-Raman or PL methods. Another way to solve this problem is to use PL and Raman spectrometers simultaneously.

As mentioned in Section 3.5, G band can also be used in characterizing the diameter of a SWCNT. However, the frequency of G band can be affected significantly by strain,[149,150] charge transfer,[151] and substrate identity.[152] The shape of G^- peak is also widely used to distinguish metallic SWCNTs and semiconducting SWCNTs. Metallic SWCNTs have an asymmetric Breit-Wigner-Fano (BWF) peak due to phonon coupling with the electronic continuum,[153] whereas semiconducting SWCNTs exhibit a symmetric Lorentzian peak.

Other Raman features, including 2D features,[55,154] intermediate frequency model (IFM) features,[155,156] and electronic Raman scattering (ERS)[157] have also been reported to characterize the chiral indices of SWCNTs, but not as widely as RBM features.

Furthermore, Raman spectroscopy can also be used in in-situ characterization. For example, Rao and co-workers reported the measurements of growth rates of individual SWCNTs through in-situ Raman measurements and correlated them with their helix angles.[25] They employed laser-induced heating of catalysts on silicon pillars, which are formed by etching Si/SiO_2 wafers. The scattered light from the pillar is used to collect Raman spectra, which are acquired continuously during the growth of a single SWCNT within the laser spot. SWCNT length is calculated by intensity of the G band at 1560 cm^{-1}. RBM is used to calculate the diameter of the SWCNT, which allows the assignment of the chiral index by the d-E_{ii} method. The relationship between helix angle and growth rate are analyzed in this work.

This method is quick, non-destructive, and the instrument is generally available to a wide community user and has become one of the most widely used and convenient ways to characterize the chirality of a SWCNT. However, due to the obstacle of measurements of large-diameter SWCNTs, some other methods should be used to locate the accurate (n, m), like PL, resonant Rayleigh spectra and ED.

6.7. Chiral Index Determined by Resonant Rayleigh Spectra

Rayleigh scattering involves an elastic scattering process, which can be greatly enhanced by the resonance effect when the incident photon energy matches the electronic transition energy.

To minimize background scattering and achieve a good signal-to-noise ratio, individual SWCNTs are suspended over a gap and illuminated by a focused laser beam.[74,158,159] In 2004, Sfeir and co-workers used standard optical lithography and wet etching procedures to prepare a slit on a silicon substrate.[74] Flow-directed SWCNTs were prepared using a chemical vapor deposition process which crossed the slit, as shown in **Figure 9**a. The supercontinuous white-light is generated by passing femtosecond laser pulses from the output of a mode-locked Ti:sapphire laser operating at a wavelength of 800 nm through a microstructured optical fiber. The nonlinear response of the fiber yields radiation covering a spectral range of ~450 to 1550 nm with an average power of tens of milliwalts. The white light is focused with a microscope on the slit and is at normal incidence to a suspended SWCNT. The scattered light is then collected at an oblique angle in a confocal arrangement. The Rayleigh scattering image on a CCD camera is shown in Figure 9b. RBM is used simultaneously to determine the diameter of the SWCNT, and the chiral indices of the SWCNT can be assigned.

Although we can get good results using this method, the suspended geometry limits its spatial resolution, the diameter range of observable nanotubes (determined by the growth method), and the correlation with other measurements (such as AFM). To overcome these problems, Joh and co-workers developed a so-called 'on-chip Rayleigh image', which realized the characterization of horizontal arrays on quartz substrates.[160] They used a broadband laser-based dark-field microscope to minimize the background scattering without suspending the SWCNTs, allowing Rayleigh imaging of SWCNTs directly on a solid substrate for the first time. As shown in Figure 9c, the substrate with SWCNTs was coated with glycerol, serving as an index-matching medium. Moreover, the laser excitation geometry prevented incident light from being collected by the detection optics. AFM heights (d_{AFM}) were measured after carefully removing the glycerol. After using a corrected experimental diameter $d = d_{AFM} + 0.2$ nm to estimate the real tube diameter, the chiral indices can be assigned via the d-E_{ii} method. On-chip Rayleigh imaging can also identify and locate sudden changes along the length direction of individual carbon nanotubes. Figure 9d shows examples of intramolecular junctions, including semiconductor–semiconductor and metal–semiconductor junctions.

small NANO MICRO

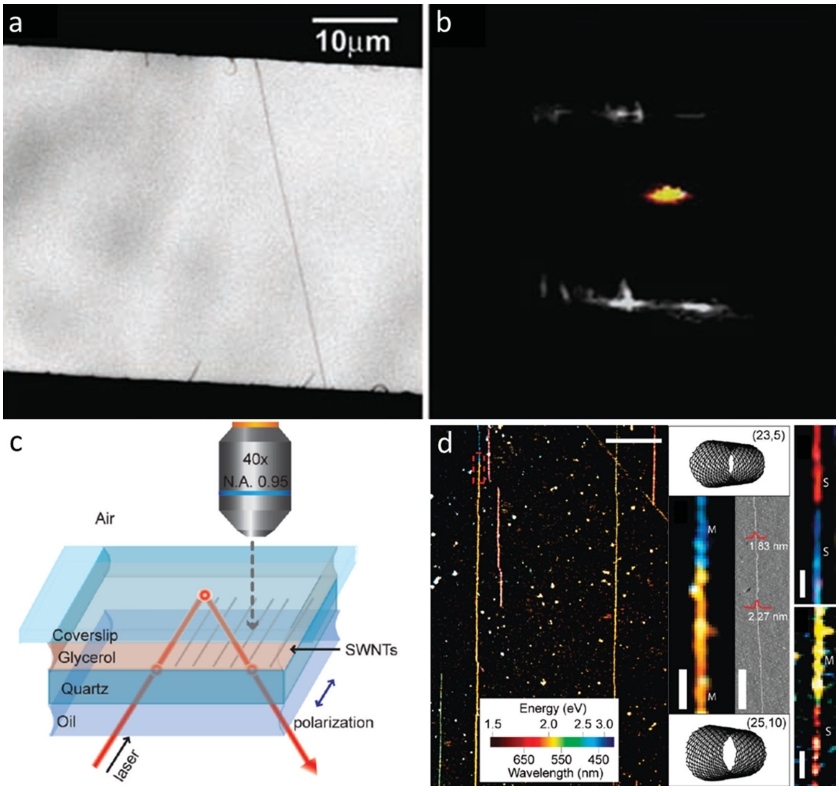

Figure 9. a) SEM image of a SWCNT on a silicon substrate. b) Rayleigh scattering imaging of the SWCNT. Reproduced with permission.[74] Copyright 2004, AAAS. c) Schematic of the optical setup of an on-chip Rayleigh image. d) Representative spatial Rayleigh images of intramolecular junctions. Reproduced with permission.[160] Copyright 2010, ACS.

Resonant Rayleigh spectroscopy provides a powerful characterization technique for individual SWCNTs, offering rapid feedback of key nanotube properties. However, the sample preparation for this method is relatively complex compared to that of resonant Raman spectroscopy. The requirement of a continuous laser is another limitation for its wide use.

6.8. Other Methods

In addition to the common imaging and spectroscopy techniques mentioned above, some special methods have also been reported for the characterization of the electronic structure of a SWCNT. Five methods—an absolute absorption cross-section method, a charge-transfer bleaching method, a photocurrent spectroscopy method, a circular dichroism method, and an X-ray diffraction method—will be introduced in this section.

6.8.1. Absolute Absorption Cross-Section

Early in 2002, the chirality dependence of SWCNT optical transition energies was established.[58] However, much less information is available for the cross sections of SWCNTs. In 2004, Islam and co-workers first reported the absorption cross section of a SWCNT of 1.7×10^{-18} cm^2 per C-atom for E_{22}.[161] The spectrum of their sample was broad and structureless, which suggested that the value is a combination of multiple unresolved absorption peaks. Because of the abundant content of (6, 5) species in CoMoCAT and HiPco samples, many groups have focused on the absorption cross section of (6, 5) SWCNTs.[162–165] In recent years, much work has been reported on the relationship between the structure and the adsorption cross section. Wang and co-workers compiled an atlas based on simultaneous electron diffraction measurements of the chiral index and Rayleigh scattering measurements of the optical resonances, which allow identification of the chiral index of a SWCNT from a measurement of its optical resonances.[166] They first realized high-throughput and quantitative determination of nanotube absorption cross-sections over a broad spectral range at a single-tube level for more than 50 individual chirality-defined SWCNTs.[167] This proved that the absolute absorption cross-section could be used to characterize the structure of SWCNTs. In 2014, Weisman and co-workers measured peaks and spectrally integrated absolute absorption cross sections for the first (E_{11}) and second (E_{22}) optical transitions of seven semiconducting SWCNT species in a bulk suspension.[168] They found that the cross sections per carbon atom decrease with increasing nanotube diameter, and E_{11} absorptions are stronger than E_{22}. However, in experiments on single SWCNTs, the attenuation measurements are still challenging,[168] which would limit its application.

6.8.2. Charge-Transfer Bleaching

UV/vis/NIR absorbance spectra have been used to monitor electron transfer between small molecule redox reagents and SWCNTs by Zheng and Diner.[162] (6, 5) SWCNTs were enriched by DNA-wrapping, and K_2IrCl_6 was used as an oxidant. Changes in the first van Hove absorbance spectra of the nanotubes were observed. The reduction potential of SWCNTs is found to increase with increasing bandgap and decrease with the introduction of an anionic dispersant. O'Connell and co-workers made a further study of the reactivity of HiPco nanotubes, suspended in SDS solution with 4-amino-1,1-azobenzene-3,4-disulphonic acid (AB).[169] Relative intensity as a function of time for fluorescence was fitted as a pseudo first-order reaction. Moreover, they noted that the near-linear dependency of the Fermi level on the bandgap directly translates to the observed near-linearity in the reaction rates. This could help to measure the electronic structure of a SWCNT.

6.8.3. Photocurrent Spectroscopy

A carbon nanotube device was fabricated starting from a piece of Si wafer covered with 285 nm thermal SiO_2 by

Barkelid and co-workers.[170] Trench gates were patterned using electron beam lithography followed by the evaporation of Pt. The carbon nanotubes were grown in a CVD oven at 900 °C under CH_4 and H_2 flow. For the photocurrent image, the reflected light from the sample was collected by a photodiode, generating a reflection image of the sample. Simultaneously, the current through the SWCNT was measured for every laser coordinate, generating the photocurrent image. External quantum efficiencies of 12.3% and 8.7% were obtained for the E_{11} and E_{22} optical resonances, respectively, and this set a lower limit for the absorption coefficient for a single semiconducting carbon nanotube. This phenomenon could also be helpful to analyze the electronic structure of a SWCNT.

6.8.4. Circular Dichroism (CD)

With the exception of structures with high symmetry (the so-called armchair and zigzag tubes), all nanotubes are chiral, that is, the tubes possess either right- or left-handed helicity. Among the methods discussed above, only STM, TEM, and graphite-assisted AFM can distinguish the right- and left-handedness of the tubes. It has been predicted that pure SWCNT enantiomers should exhibit circular dichroism (CD).[30,171,172] Dukovic and co-workers showed that a racemic mixture of nanotubes exhibits CD when the SWCNTs are wrapped with DNA.[173] In the corresponding CD spectrum, peaks associated with the E_{ii} transitions are clearly evident, which can be used to assign the chiral index. Nanotubes solubilized with sodium dodecyl benzenesulfonate (NaDDBS), a nonchiral surfactant, do not exhibit CD. This suggests that either wrapping selects one nanotube enantiomer over the other, the observation of CD signal is inherent to a chiral nanotube, or the inherent chirality of DNA induces the CD signal in a racemic mixture of SWCNTs. This offers a way to characterize the helicity of a SWCNT.

6.8.5. X-Ray Diffraction

In addition to electronic diffraction, X-ray diffraction (XRD) can also afford a geometrical determination of SWCNT. Powder XRD measurements were carried out to determine the effectiveness of the proposed method. Highly enriched SWCNTs with certain chiralities were prepared from a purchased SWCNT material using a combination of gel-separation[174] and density gradient ultracentrifugation purification[175,176] techniques. Powder XRD patterns were then observed for the purified samples. The measurements were performed using synchrotron radiation with a wavelength of 1 Å at beam lines. The SWCNT sample was sealed in vacuum inside a quartz tube after thorough evacuation at 770 K to remove materials adsorbed both inside and outside the SWCNTs.[177] The fine structures appear around $Q > 5$ (1/Å) region, depending on the SWCNT sample's chirality distribution. The analysis of the fine structure is discussed in detail in reference [178], and will not be described here.

7. Conclusion

The geometry, expressed by chiral index (n, m) of SWCNTs, plays an important role in determining their structure-related properties. Depending on different mechanisms, imaging techniques and spectroscopy techniques can be used to probe (n, m). **Table 3** shows the substrate of the methods mentioned above.

As compared with spectroscopy techniques, imaging techniques are more relevant and direct for the characterization of individual SWCNTs independently. STM and TEM provide atomic-resolution graphs and structures of defects, and ends can be observed as well. Furthermore, left- and right-handed SWCNTs can be distinguished by these methods. ED can be used to characterize the structure of each layer in multiwalled tubes, especially double-walled tubes, from the diffraction pattern. These methods can characterize any given structure of a SWCNT, which is independent of the structure of electric or phonon. However, the problem with these methods is that the sample preparation is very complicated. Special substrates or suspended conditions are often required, and an ultrahigh vacuum system is also needed. Being treated with high voltage or an electron beam, samples are easily damaged. Furthermore, imaging techniques usually require long data acquisition times, which limit their use as a general large-area or large-amount characterization method for arrays or powder-like SWCNTs.

Most spectroscopy techniques can work at room temperature and under atmospheric conditions, and the sample preparation is simple. Optical images of SWCNTs allow rapid and easy visualization. The quick response time and convenient sample movement make it easy to realize large-area mapping, which is useful for characterizing SWCNT arrays. Meanwhile, the measurement procedure is usually noninvasive to the sample. Spectroscopy techniques also have their limitations. Firstly, the accuracy of determination is relatively poor for large-diameter SWCNTs, which can be explained as the decreasing of $\Delta(1/d)$ when d increases. Hence two or more methods are usually required to ensure accuracy. Secondly, some spectroscopy techniques only work for certain material types, for example, PL can only characterize semiconducting SWCNTs, and single-wavelength Raman spectroscopy can only characterize parts of resonant tubes. That is to say, spectroscopy, especially Raman, is mostly used to obtain statistical results on a large amount of samples. Imaging techniques like ED, however, are good at characterizing one SWCNT with visual information, and can also provide convincing evidence of (n, m) as a supplement of spectroscopy.

Table 3. Substrates of the different methods.

Substrate	Example	Method
Amorphous	$Si(SiO_2$ coating);Glass coverslip	AFM, Raman, FL, RRS
Lattice with interaction	Sapphire; Graphite	Raman, AFM, STM
Lattice without interaction	Au(111)	STM
Suspended	——	TEM, SAED, Raman, FL, RRS
Solution	Aqueous	FL

NANO MICRO small

Though many constructive works have been reported in the past 20 years, comprehensive and accurate methods to conveniently determine the (n, m) structure of any given SWCNT is still a great challenge. More structure-related properties should be in-depth understood, so as to develop new methodologies and techniques. Thus, the room for improvement is still broad, and more effort is still needed.

Acknowledgements

This work was supported by NSFC (21233001, 21129001, 51272006 and 51121091) and MOST (2011CB932601).

[1] S. Iijima, T. Ichihashi, *Nature* **1993**, *364*, 737.
[2] R. Saito, G. Dresselhaus, M. S. Dresselhaus, *Physical Properties of Carbon Nanotubes*, World Scientific, London **1998**, Vol. *4*.
[3] S. J. Tans, A. R. Verschueren, C. Dekker, *Nature* **1998**, *393*, 49.
[4] Z. Chen, J. Appenzeller, Y.-M. Lin, J. Sippel-Oakley, A. G. Rinzler, J. Tang, S. J. Wind, P. M. Solomon, P. Avouris, *Science* **2006**, *311*, 1735.
[5] M. F. De Volder, S. H. Tawfick, R. H. Baughman, A. J. Hart, *Science* **2013**, *339*, 535.
[6] M. Briman, E. Artukovic, L. Zhang, D. Chia, L. Goodglick, G. Gruner, *Small* **2007**, *3*, 758.
[7] D. S. Bethune, C. H. Kiang, M. S. Devries, G. Gorman, R. Savoy, J. Vazquez, R. Beyers, *Nature* **1993**, *363*, 605.
[8] A. Thess, R. Lee, P. Nikolaev, H. Dai, P. Petit, J. Robert, C. Xu, Y. H. Lee, S. G. Kim, A. G. Rinzler, *Science* **1996**, *273*, 483.
[9] P. Nikolaev, M. J. Bronikowski, R. K. Bradley, F. Rohmund, D. T. Colbert, K. A. Smith, R. E. Smalley, *Chem. Phys. Lett.* **1999**, *313*, 91.
[10] M. Su, B. Zheng, J. Liu, *Chem. Phys. Lett.* **2000**, *322*, 321.
[11] N. Geblinger, A. Ismach, E. Joselevich, *Nat. Nanotechnol.* **2008**, *3*, 195.
[12] Y. G. Yao, C. Q. Feng, J. Zhang, Z. F. Liu, *Nano Lett.* **2009**, *9*, 1673.
[13] A. Ismach, E. Joselevich, *Nano Lett.* **2006**, *6*, 1706.
[14] C. Kocabas, M. Shim, J. A. Rogers, *J. Am. Chem. Soc.* **2006**, *128*, 4540.
[15] L. Ding, D. N. Yuan, J. Liu, *J. Am. Chem. Soc.* **2008**, *130*, 5428.
[16] K. Hata, D. N. Futaba, K. Mizuno, T. Namai, M. Yumura, S. Iijima, *Science* **2004**, *306*, 1362.
[17] Q. Li, X. Zhang, R. F. DePaula, L. Zheng, Y. Zhao, L. Stan, T. G. Holesinger, P. N. Arendt, D. E. Peterson, Y. T. Zhu, *Adv. Mater.* **2006**, *18*, 3160.
[18] S. S. Fan, M. G. Chapline, N. R. Franklin, T. W. Tombler, A. M. Cassell, H. J. Dai, *Science* **1999**, *283*, 512.
[19] S. M. Huang, X. Y. Cai, J. Liu, *J. Am. Chem. Soc.* **2003**, *125*, 5636.
[20] A. J. Hart, A. H. Slocum, *J. Phys. Chem. B* **2006**, *110*, 8250.
[21] X. S. Wang, Q. Q. Li, J. Xie, Z. Jin, J. Y. Wang, Y. Li, K. L. Jiang, S. S. Fan, *Nano Lett.* **2009**, *9*, 3137.
[22] J. Li, Y. J. He, Y. M. Han, K. Liu, J. P. Wang, Q. Q. Li, S. S. Fan, K. L. Jiang, *Nano Lett.* **2012**, *12*, 4095.
[23] R. F. Zhang, Y. Y. Zhang, Q. Zhang, H. H. Xie, H. D. Wang, J. Q. Nie, Q. Wen, F. Wei, *Nature Commun.* **2013**, *4*,1727.
[24] L. Mleczko, G. Lolli, *Angew. Chem. Int. Ed.* **2013**, *52*, 9372.
[25] R. Rao, D. Liptak, T. Cherukuri, B. I. Yakobson, B. Maruyama, *Nat. Mater.* **2012**, *11*, 213.
[26] Y. Yao, Q. Li, J. Zhang, R. Liu, L. Jiao, Y. T. Zhu, Z. Liu, *Nat. Mater.* **2007**, *6*, 283.
[27] Y. G. Yao, X. C. Dai, R. Liu, J. Zhang, Z. F. Liu, *J. Phys. Chem. C* **2009**, *113*, 13051.
[28] M. S. Dresselhaus, G. Dresselhaus, P. C. Eklund, *Science of Fullerenes and Carbon Nanotubes: Their Properties and Applications*, Academic Press, Amsterdam, **1996**.
[29] M. Dresselhaus, G. Dresselhaus, R. Saito, *Phys. Rev. B* **1992**, *45*, 6234.
[30] G. G. Samsonidze, A. Grüneis, R. Saito, A. Jorio, A. Souza Filho, G. Dresselhaus, M. Dresselhaus, *Phys. Rev. B* **2004**, *69*, 205402.
[31] M. S. Dresselhaus, G. Dresselhaus, R. Saito, A. Jorio, *Phys. Rep.* **2005**, *409*, 47.
[32] Y. Chen, Y. Hu, M. Liu, W. Xu, Y. Zhang, L. Xie, J. Zhang, *Nano Lett.* **2013**, *13*, 5666.
[33] G. G. Samsonidze, A. Saito, D. Jorio, E. Pimenta, F. Souza, F. Grüneis, D. Dresselhaus, M. Dresselhausa, *J. Nanosci. Nanotechnol.* **2003**, *3*, 431.
[34] T. W. Odom, J.-L. Huang, P. Kim, C. M. Lieber, *Nature* **1998**, *391*, 62.
[35] S. Reich, C. Thomsen, *Phys. Rev. B* **2000**, *62*, 4273.
[36] R. Saito, G. Dresselhaus, M. Dresselhaus, *Phys. Rev. B* **2000**, *61*, 2981.
[37] J. Maultzsch, S. Reich, C. Thomsen, H. Requardt, P. Ordejón, *Phys. Rev. Lett.* **2004**, *92*, 075501.
[38] A. Jorio, R. Saito, J. Hafner, C. Lieber, M. Hunter, T. McClure, G. Dresselhaus, M. Dresselhaus, *Phys. Rev. Lett.* **2001**, *86*, 1118.
[39] C. Kocabas, S. H. Hur, A. Gaur, M. A. Meitl, M. Shim, J. A. Rogers, *Small* **2005**, *1*, 1110.
[40] K. Seong Jun, C. Kocabas, T. Ozel, M. Shim, N. Pimparkar, M. A. Alam, S. V. Rotkin, J. A. Rogers, *Nat. Nanotechnol.* **2007**, *2*, 230.
[41] L. Ding, D. Yuan, J. Liu, *J. Am. Chem. Soc.* **2008**, *130*, 5428.
[42] H. Ago, K. Nakamura, K. Ikeda, N. Uehara, N. Ishigami, M. Tsuji, *Chem. Phys. Lett.* **2005**, *408*, 433.
[43] S. Han, X. L. Liu, C. W. Zhou, *J. Am. Chem. Soc.* **2005**, *127*, 5294.
[44] N. Ishigami, H. Ago, K. Imamoto, M. Tsuji, K. Iakoubovskii, N. Minami, *J. Am. Chem. Soc.* **2008**, *130*, 9918.
[45] Y. Chen, Z. Shen, Z. Xu, Y. Hu, H. Xu, S. Wang, X. Guo, Y. Zhang, L. Peng, F. Ding, *Nature Commun.* **2013**, *4*,1
[46] C. Gerber, H. P. Lang, *Nat. Nanotechnol.* **2006**, *1*, 3.
[47] H. Ago, N. Ishigami, N. Yoshihara, K. Imamoto, S. Akita, K.-I. Ikeda, M. Tsuji, T. Ikuta, K. Takahashi, *J. Phys. Chem. C* **2008**, *112*, 1735.
[48] G. Binnig, H. Rohrer, C. Gerber, E. Weibe, *Appl. Phys. Lett* **1982**, *40*, 178.
[49] A. Hashimoto, K. Suenaga, A. Gloter, K. Urita, S. Iijima, *Nature* **2004**, *430*, 870.
[50] T. W. Odom, J. L. Huang, P. Kim, M. Ouyang, C. M. Lieber, *J. Mater. Res.* **1998**, *13*, 2380.
[51] L. C. Qin, *J. Mater. Res.* **1994**, *9*, 2450.
[52] L.-C. Qin, *Phys. Chem. Chem. Phys.* **2007**, *9*, 31.
[53] M. Gao, J. M. Zuo, R. D. Twesten, I. Petrov, L. A. Nagahara, R. Zhang, *Appl. Phys. Lett.* **2003**, *82*, 2703.
[54] A. Souza Filho, A. Jorio, G. G. Samsonidze, G. Dresselhaus, M. Pimenta, M. Dresselhaus, A. K. Swan, M. Ünlü, B. Goldberg, R. Saito, *Phys. Rev. B* **2003**, *67*, 035427.
[55] A. Jorio, A. Souza Filho, G. Dresselhaus, M. Dresselhaus, A. Swan, M. Ünlü, B. Goldberg, M. Pimenta, J. Hafner, C. Lieber, *Phys. Rev. B* **2002**, *65*, 155412.
[56] A. Jorio, M. Pimenta, A. Souza Filho, G. G. Samsonidze, A. Swan, M. Ünlü, B. Goldberg, R. Saito, G. Dresselhaus, M. Dresselhaus, *Phys. Rev. Lett.* **2003**, *90*, 107403.
[57] V. Brar, G. G. Samsonidze, M. Dresselhaus, G. Dresselhaus, R. Saito, A. Swan, M. Ünlü, B. Goldberg, A. Souza Filho, A. Jorio, *Phys. Rev. B* **2002**, *66*, 155418.
[58] S. M. Bachilo, M. S. Strano, C. Kittrell, R. H. Hauge, R. E. Smalley, R. B. Weisman, *Science* **2002**, *298*, 2361.
[59] J. C. Meyer, M. Paillet, T. Michel, A. Moreac, A. Neumann, G. S. Duesberg, S. Roth, J. L. Sauvajol, *Phys. Rev. Lett.* **2005**, *95*, 4.

[60] A. Jungen, V. N. Popov, C. Stampfer, L. Durrer, S. Stoll, C. Hierold, *Phys. Rev. B* **2007**, *75*, 4.
[61] P. T. Araujo, I. Maciel, P. Pesce, M. Pimenta, S. Doorn, H. Qian, A. Hartschuh, M. Steiner, L. Grigorian, K. Hata, *Phys. Rev. B* **2008**, *77*, 241403.
[62] K. Liu, W. Wang, M. Wu, F. Xiao, X. Hong, S. Aloni, X. Bai, E. Wang, F. Wang, *Phys. Rev. B* **2011**, *83*, 113404.
[63] G. D. Mahan, *Phys. Rev. B* **2002**, *65*, 7.
[64] J. H. Warner, N. P. Young, A. I. Kirkland, G. A. D. Briggs, *Nat. Mater.* **2011**, *10*, 958.
[65] C. Allen, C. Zhang, G. Burnell, A. Brown, J. Robertson, B. Hickey, *Carbon* **2011**, *49*, 4961.
[66] D. G. de Oteyza, P. Gorman, Y.-C. Chen, S. Wickenburg, A. Riss, D. J. Mowbray, G. Etkin, Z. Pedramrazi, H.-Z. Tsai, A. Rubio, M. F. Crommie, F. R. Fischer, *Science* **2013**, *340*, 1434.
[67] J. Zhang, P. C. Chen, B. K. Yuan, W. Ji, Z. H. Cheng, X. H. Qiu, *Science* **2013**, *342*, 611.
[68] S. Han, X. Liu, C. Zhou, *J. Am. Chem. Soc.* **2005**, *127*, 5294.
[69] Y. Chen, Y. Hu, Y. Fang, P. Li, C. Feng, J. Zhang, *Carbon* **2012**, *50*, 3295.
[70] J. A. Stroscio, W. J. Kaiser, *Scanning Tunneling Microscopy*, Academic Press, Amsterdam **1993**, Vol. *27*.
[71] J. W. Wilder, L. C. Venema, A. G. Rinzler, R. E. Smalley, C. Dekker, *Nature* **1998**, *391*, 59.
[72] L. Cançado, M. Pimenta, R. Saito, A. Jorio, L. Ladeira, A. Grueneis, A. Souza-Filho, G. Dresselhaus, M. Dresselhaus, *Phys. Rev. B* **2002**, *66*, 035415.
[73] B. Jusserand, M. Cardona, in *Light Scattering in Solids V*, Springer, Berlin, **1989**, p.49.
[74] M. Y. Sfeir, F. Wang, L. Huang, C.-C. Chuang, J. Hone, S. P. O'Brien, T. F. Heinz, L. E. Brus, *Science* **2004**, *306*, 1540.
[75] J. Wildöer, A. Van Roy, H. Van Kempen, C. Harmans, *Rev. Sci. Instrum.* **1994**, *65*, 2849.
[76] M. P. Everson, R. C. Jaklevic, W. D. Shen, *J. Vacuum Sci. Technol.* **1990**, *8*, 3662.
[77] J. Xue, J. Sanchez-Yamagishi, D. Bulmash, P. Jacquod, A. Deshpande, K. Watanabe, T. Taniguchi, P. Jarillo-Herrero, B. J. LeRoy, *Nat. Mater.* **2011**, *10*, 282.
[78] T. W. Odom, J.-L. Huang, P. Kim, C. M. Lieber, *J. Phys. Chem. B* **2000**, *104*, 2794.
[79] A. Hassanien, M. Tokumoto, Y. Kumazawa, H. Kataura, Y. Maniwa, S. Suzuki, Y. Achiba, *Appl. Phys. Lett.* **1998**, *73*, 3839.
[80] M. R. Falvo, R. M. Taylor, A. Helser, V. Chi, F. P. Brooks, S. Washburn, R. Superfine, *Nature* **1999**, *397*, 236.
[81] S. S. Wong, A. T. Woolley, T. W. Odom, J. L. Huang, P. Kim, D. V. Vezenov, C. M. Lieber, *Appl. Phys. Lett.* **1998**, *73*, 3465.
[82] P. Lambin, A. A. Lucas, J. C. Charlier, *J. Phys. Chem. Solids* **1997**, *58*, 1833.
[83] L. Chico, V. H. Crespi, L. X. Benedict, S. G. Louie, M. L. Cohen, *Phys. Rev. Lett.* **1996**, *76*, 971.
[84] V. Meunier, L. Henrard, P. Lambin, *Phys. Rev. B* **1998**, *57*, 2586.
[85] J. Han, M. P. Anantram, R. L. Jaffe, J. Kong, H. Dai, *Phys. Rev. B* **1998**, *57*, 14983.
[86] P. Kim, T. W. Odom, J. L. Huang, C. M. Lieber, *Phys. Rev. Lett.* **1999**, *82*, 1225.
[87] M. Ouyang, J.-L. Huang, C. L. Cheung, C. M. Lieber, *Science* **2001**, *291*, 97.
[88] M. He, H. Jiang, B. Liu, P. V. Fedotov, A. I. Chernov, E. D. Obraztsova, F. Cavalca, J. B. Wagner, T. W. Hansen, I. V. Anoshkin, *Sci. Rep.* **2013**, *3*,1.
[89] H. Yoshida, S. Takeda, T. Uchiyama, H. Kohno, Y. Homma, *Nano Lett.* **2008**, *8*, 2082.
[90] C. Allen, M. Elkin, C. Zhang, S. Hofmann, G. Burnell, J. Robertson, B. Hickey, in Journal of Physics: Conference Series, IOP Publishing, Bristol, **2010**, 012082.
[91] H. Seidel, L. Csepregi, A. Heuberger, H. Baumgartel, *J. Electrochem. Soc.* **1990**, *137*, 3612.
[92] A. Stone, D. Wales, *Chem. Phys. Lett.* **1986**, *128*, 501.
[93] R. H. Telling, C. P. Ewels, A. Ahlam, M. I. Heggie, *Nat. Mater.* **2003**, *2*, 333.
[94] A. El-Barbary, R. Telling, C. Ewels, M. Heggie, P. Briddon, *Phys. Rev. B* **2003**, *68*, 144107.
[95] A. Krasheninnikov, K. Nordlund, P. Lehtinen, A. Foster, A. Ayuela, R. Nieminen, *Phys. Rev. B* **2004**, *69*, 073402.
[96] K. Nordlund, J. Keinonen, T. Mattila, *Phys. Rev. Lett.* **1996**, *77*, 699.
[97] P. Lehtinen, A. Foster, A. Ayuela, A. Krasheninnikov, K. Nordlund, R. Nieminen, *Phys. Rev. Lett.* **2003**, *91*, 017202.
[98] K. Suenaga, H. Wakabayashi, M. Koshino, Y. Sato, K. Urita, S. Iijima, *Nat. Nanotechnol.* **2007**, *2*, 358.
[99] J. H. Warner, F. Schäffel, G. Zhong, M. H. Rummeli, B. Buchner, J. Robertson, G. A. D. Briggs, *ACS Nano* **2009**, *3*, 1557.
[100] C. Jin, K. Suenaga, S. Iijima, *Nano Lett.* **2008**, *8*, 1127.
[101] K. M. Kadish, R. S. Ruoff, *Electrochem. Soc.*, **1997**, *9*, 42.
[102] M. B. Nardelli, B. Yakobson, J. Bernholc, *Phys. Rev. B* **1998**, *57*, R4277.
[103] Y. Xia, Y. Ma, Y. Xing, Y. Mu, C. Tan, L. Mei, *Phys. Rev. B* **2000**, *61*, 11088.
[104] T. Dumitrica, M. Hua, B. I. Yakobson, *Proc. Natl. Acad. Sci.* **2006**, *103*, 6105.
[105] R. Egerton, P. Li, M. Malac, *Micron* **2004**, *35*, 399.
[106] A. Krasheninnikov, F. Banhart, *Nat. Mater.* **2007**, *6*, 723.
[107] Y. Sato, K. Yanagi, Y. Miyata, K. Suenaga, H. Kataura, S. Iijima, *Nano Lett.* **2008**, *8*, 3151.
[108] L.-C. Qin, S. Iijima, H. Kataura, Y. Maniwa, S. Suzuki, Y. Achiba, *Chem. Phys. Lett.* **1997**, *268*, 101.
[109] J. Cowley, P. Nikolaev, A. Thess, R. E. Smalley, *Chem. Phys. Lett.* **1997**, *265*, 379.
[110] P. B. Hirsch, A. Howie, R. Nicholson, D. Pashley, M. J. Whelan, *Electron Microscopy of Thin Crystals*, Butterworths, London, **1965**, Vol. *320*.
[111] S. Amelinckx, A. Lucas, P. Lambin, *Rep. Prog. Phys.* **1999**, *62*, 1471.
[112] Z. Liu, Q. Zhang, L.-C. Qin, *Appl. Phys. Lett.* **2005**, *86*, 191903.
[113] K. Hirahara, K. Inose, Y. Nakayama, *Appl. Phys. Lett.* **2010**, *97*,051905.
[114] M. S. He, B. L. Liu, A. I. Chernov, E. D. Obraztsova, I. Kauppi, H. Jiang, I. Anoshkin, F. Cavalca, T. W. Hansen, J. B. Wagner, A. G. Nasibulin, E. I. Kauppinen, J. Linnekoski, M. Niemela, J. Lehtonen, *Chem. Mater.* **2012**, *24*, 1796.
[115] C. S. Allen, M. D. Elkin, G. Burnell, B. J. Hickey, C. Zhang, S. Hofmann, J. Robertson, *Phys. Rev. B* **2011**, *84*,115444.
[116] R. Arenal, P. Lothman, M. Picher, T. Than, M. Paillet, V. Jourdain, *J. Phys. Chem. C* **2012**, *116*, 14103.
[117] M. Y. Sfeir, T. Beetz, F. Wang, L. M. Huang, X. M. H. Huang, M. Y. Huang, J. Hone, S. O'Brien, J. A. Misewich, T. F. Heinz, L. J. Wu, Y. M. Zhu, L. E. Brus, *Science* **2006**, *312*, 554.
[118] Z. Liu, L.-C. Qin, *Chem. Phys. Lett.* **2005**, *406*, 106.
[119] Z. Liu, L.-C. Qin, *Chem. Phys. Lett.* **2004**, *400*, 430.
[120] T. Kim, G. Kim, W. I. Choi, Y.-K. Kwon, J.-M. Zuo, *Appl. Phys. Lett.* **2010**, *96*, 173107.
[121] J. Zhang, J. Zuo, *Carbon* **2009**, *47*, 3515.
[122] Y. Jiang, W. Zhou, T. Kim, Y. Huang, J. Zuo, *Phys. Rev. B* **2008**, *77*, 153405.
[123] Q. Wen, W. Qian, J. Nie, A. Cao, G. Ning, Y. Wang, L. Hu, Q. Zhang, J. Huang, F. Wei, *Adv. Mater.* **2010**, *22*, 1867.
[124] J. Zuo, I. Vartanyants, M. Gao, R. Zhang, L. Nagahara, *Science* **2003**, *300*, 1419.
[125] R. P. Millane, W. J. Stroud, *J. Optical Soc. Am. A* **2003**, *14*, 568.
[126] H. Deniz, A. Derbakova, L. C. Qin, *Ultramicroscopy* **2010**, *111*, 66.
[127] J.-F. Colomer, L. Henrard, P. Launois, G. Van Tendeloo, A. Lucas, P. Lambin, *Phys. Rev. B* **2004**, *70*, 075408.

NANO MICRO small

[128] M. Falvo, J. Steele, I. RM Taylor, R. Superfine, *Phys. Rev. B* **2000**, *62*, R10665.
[129] M. Seydou, S. Marsaudon, J. Buchoux, J. P. Aimé, A. M. Bonnot, *Phys. Rev. B* **2009**, *80*, 245421.
[130] A. N. Kolmogorov, V. H. Crespi, *Phys. Rev. B* **2005**, *71*, 235415.
[131] M. J. O'connell, S. M. Bachilo, C. B. Huffman, V. C. Moore, M. S. Strano, E. H. Haroz, K. L. Rialon, P. J. Boul, W. H. Noon, C. Kittrell, *Science* **2002**, *297*, 593.
[132] O. N. Torrens, D. E. Milkie, M. Zheng, J. M. Kikkawa, *Nano Lett.* **2006**, *6*, 2864.
[133] P. Tan, A. Rozhin, T. Hasan, P. Hu, V. Scardaci, W. Milne, A. Ferrari, *Phys. Rev. Lett.* **2007**, *99*, 137402.
[134] J. Lefebvre, P. Finnie, *J. Phys. Chem. C* **2009**, *113*, 7536.
[135] S. Reich, J. Maultzsch, C. Thomsen, P. Ordejon, *Phys. Rev. B* **2002**, *66*, 035412.
[136] Y. Oyama, R. Saito, K. Sato, J. Jiang, G. G. Samsonidze, A. Grüneis, Y. Miyauchi, S. Maruyama, A. Jorio, G. Dresselhaus, *Carbon* **2006**, *44*, 873.
[137] D. A. Tsyboulski, J.-D. R. Rocha, S. M. Bachilo, L. Cognet, R. B. Weisman, *Nano Lett.* **2007**, *7*, 3080.
[138] D. A. Heller, R. M. Mayrhofer, S. Baik, Y. V. Grinkova, M. L. Usrey, M. S. Strano, *J. Am. Chem. Soc.* **2004**, *126*, 14567.
[139] S.-Y. Ju, W. P. Kopcha, F. Papadimitrakopoulos, *Science* **2009**, *323*, 1319.
[140] D. H. Shin, J.-E. Kim, H. C. Shim, J.-W. Song, J.-H. Yoon, J. Kim, S. Jeong, J. Kang, S. Baik, C.-S. Han, *Nano Lett.* **2008**, *8*, 4380.
[141] Y. Maeda, S. Kimura, M. Kanda, Y. Hirashima, T. Hasegawa, T. Wakahara, Y. F. Lian, T. Nakahodo, T. Tsuchiya, T. Akasaka, J. Lu, X. W. Zhang, Z. X. Gao, Y. P. Yu, S. Nagase, S. Kazaoui, N. Minami, T. Shimizu, H. Tokumoto, R. Saito, *J. Am. Chem. Soc.* **2005**, *127*, 10287.
[142] C. Wei-Hung, R. M. Sankaran, *Nat. Mater.* **2009**, *8*, 882.
[143] A. Hartschuh, H. N. Pedrosa, L. Novotny, T. D. Krauss, *Science* **2003**, *301*, 1354.
[144] K. Kono, D. Matsumoto, S. Chiashi, Y. Homma, *Surf. Interface Anal.* **2012**, *44*, 686.
[145] N. Stürzl, S. Lebedkin, F. Peng, Y. Li, F. Hennrich, M. M. Kappes, *Rev. Sci. Instrum.* **2012**, *83*, 063709.
[146] M. Steiner, M. Freitag, J. C. Tsang, V. Perebeinos, A. A. Bol, A. V. Failla, P. Avouris, *Appl. Phys. A* **2009**, *96*, 271.
[147] P. Araujo, A. Jorio, *phys. status solidi (b)* **2008**, *245*, 2201.
[148] D. Zhang, J. Yang, Y. Li, *Small* **2013**, *9*, 1284.
[149] Z. Liu, J. Zhang, B. Gao, *Chem. Commun.* **2009**, 6902.
[150] S. Cronin, A. Swan, M. Ünlü, B. Goldberg, M. Dresselhaus, M. Tinkham, *Phys. Rev. Lett.* **2004**, *93*, 167401.
[151] T. Takenobu, T. Takano, M. Shiraishi, Y. Murakami, M. Ata, H. Kataura, Y. Achiba, Y. Iwasa, *Nat. Mater.* **2003**, *2*, 683.
[152] L. Ding, W. Zhou, T. P. McNicholas, J. Wang, H. Chu, Y. Li, J. Liu, *Nano Research* **2009**, *2*, 903.
[153] S. Brown, A. Jorio, P. Corio, M. Dresselhaus, G. Dresselhaus, R. Saito, K. Kneipp, *Phys. Rev. B* **2001**, *63*, 155414.
[154] A. Souza Filho, A. Jorio, G. G. Samsonidze, G. Dresselhaus, M. Dresselhaus, A. K. Swan, M. Ünlü, B. Goldberg, R. Saito, J. Hafner, *Chem. Phys. Lett.* **2002**, *354*, 62.
[155] J. Wang, J. Yang, D. Zhang, Y. Li, *J. Phys. Chem. C* **2012**, *116*, 23826.
[156] C. Fantini, A. Jorio, M. Souza, R. Saito, G. G. Samsonidze, M. Dresselhaus, M. Pimenta, *Phys. Rev. B* **2005**, *72*, 085446.
[157] H. Farhat, S. Berciaud, M. Kalbac, R. Saito, T. Heinz, M. Dresselhaus, J. Kong, *Phys. Rev. Lett.* **2011**, *107*, 157401.
[158] F. Wang, M. Y. Sfeir, L. Huang, X. H. Huang, Y. Wu, J. Kim, J. Hone, S. O'Brien, L. E. Brus, T. F. Heinz, *Phys. Rev. Lett.* **2006**, *96*, 167401.
[159] M. Y. Sfeir, T. Beetz, F. Wang, L. Huang, X. H. Huang, M. Huang, J. Hone, S. O'Brien, J. Misewich, T. F. Heinz, *Science* **2006**, *312*, 554.
[160] D. Y. Joh, L. H. Herman, S.-Y. Ju, J. Kinder, M. A. Segal, J. N. Johnson, G. K. Chan, J. Park, *Nano Lett.* **2010**, *11*, 1.
[161] M. F. Islam, D. E. Milkie, C. L. Kane, A. G. Yodh, J. M. Kikkawa, *Phys. Rev. Lett.* **2004**, *93*,037404.
[162] M. Zheng, B. A. Diner, *J. Am. Chem. Soc.* **2004**, *126*, 15490.
[163] F. Schoppler, C. Mann, T. C. Hain, F. M. Neubauer, G. Privitera, F. Bonaccorso, D. P. Chu, A. C. Ferrari, T. Hertel, *J. Phys. Chem. C* **2011**, *115*, 14682.
[164] S. Berciaud, L. Cognet, B. Lounis, *Phys. Rev. Lett.* **2008**, *101*,077402.
[165] F. Vialla, C. Roquelet, B. Langlois, G. Delport, S. M. Santos, E. Deleporte, P. Roussignol, C. Delalande, C. Voisin, J. S. Lauret, *Phys. Rev. Lett.* **2013**, *111*.
[166] L. Kaihui, J. Deslippe, X. Fajun, R. B. Capaz, H. Xiaoping, S. Aloni, A. Zettl, W. Wenlong, B. Xuedong, S. G. Louie, W. Enge, W. Feng, *Nat. Nanotechnol.* **2012**, *7*, 325.
[167] K. H. Liu, X. P. Hong, S. Choi, C. H. Jin, R. B. Capaz, J. Kim, W. L. Wang, X. D. Bai, S. G. Louie, E. G. Wang, F. Wang, *Proc. Natl. Acad. Sci. USA* **2014**, *111*, 7564.
[168] J. K. Streit, S. M. Bachilo, S. Ghosh, C. W. Lin, R. B. Weisman, *Nano Lett.* **2014**, *14*, 1530.
[169] M. J. O'Connell, E. E. Eibergen, S. K. Doorn, *Nat. Mater.* **2005**, *4*, 412.
[170] E. Ivchenko, B. Spivak, *Phys. Rev. B* **2002**, *66*, 155404.
[171] A. Sánchez-Castillo, C. Román-Velázquez, C. Noguez, *Phys. Rev. B* **2006**, *73*, 045401.
[172] S. Tasaki, K. Maekawa, T. Yamabe, *Phys. Rev. B* **1998**, *57*, 9301.
[173] G. Dukovic, M. Balaz, P. Doak, N. D. Berova, M. Zheng, R. S. Mclean, L. E. Brus, *J. Am. Chem. Soc.* **2006**, *128*, 9004.
[174] H. Liu, D. Nishide, T. Tanaka, H. Kataura, *Nature Commun.* **2011**, *2*, 309.
[175] M. S. Arnold, A. A. Green, J. F. Hulvat, S. I. Stupp, M. C. Hersam, *Nat. Nanotechnol.* **2006**, *1*, 60.
[176] K. Yanagi, Y. Miyata, H. Kataura, *Appl. Phys. Express* **2008**, *1*, 034003.
[177] Y. Maniwa, R. Fujiwara, H. Kira, H. Tou, H. Kataura, S. Suzuki, Y. Achiba, E. Nishibori, M. Takata, M. Sakata, *Phys. Rev. B* **2001**, *64*, 241402.
[178] R. Mitsuyama, S. Tadera, H. Kyakuno, R. Suzuki, H. Ishii, Y. Nakai, Y. Miyata, K. Yanagi, H. Kataura, Y. Maniwa, *Carbon* **2014**, *75*, 299.

Received: May 31, 2014
Revised: September 12, 2014
Published online: October 20, 2014

